Cryo-EM structures of CCHFV polymerase reveal a stepwise initiation stabilization pathway and a dual-site inhibition mechanism

Kankan Yang (杨侃侃),[1,4] Haiqiang Wu (吴海强),[1,2,4] Xunbi Liu (刘勋碧),[1,2,4] Zuxing Liang (梁祖兴),[1,3] Junwei Zou (邹俊伟),[1] Yong Wang (王勇),[2] Jun Ma (马军)[1,5,*]

[1]Institute of Infectious Diseases, Shenzhen Bay Laboratory, Shenzhen, Guangdong 518132, China

[2]College of Veterinary Medicine, Anhui Agricultural University, Hefei, Anhui 230036, China

[3]College of Life Science, Capital Normal University, Beijing 100048, China

[4]These authors contributed equally

[5]Lead contact

*Correspondence: majun@szbl.ac.cn (J.M.)

SUMMARY

Crimean-Congo hemorrhagic fever virus (CCHFV) is a high-priority pathogen with high case-fatality rates, yet approved therapeutics remain unavailable. The CCHFV L segment encodes a ~450-kDa RNA-dependent RNA polymerase (L protein) orchestrating viral replication, but its structural mechanisms remain elusive. Here, we present high-resolution cryo-EM structures of the CCHFV L protein in apo, 5' vRNA-bound, 5'/3' promoter-bound, and inhibitor-bound states. The catalytic core exhibits the canonical architecture of the *Bunyavirales* order, featuring conserved motifs and coordinated promoter recognition via a 5' vRNA "hook" and a secondary 3' vRNA-binding site. Using suramin as a probe, we identified a dual-site mechanism of polymerase inhibition. Suramin competitively occludes the 5' vRNA-binding pocket through electrostatic mimicry of the RNA backbone and concurrently traps a distal Linker–Fingers interface, restricting the conformational dynamics required for catalysis. Collectively, these findings provide structural insights into CCHFV polymerase regulation and inhibition.

KEY WORDS

Crimean-Congo hemorrhagic fever virus, RNA-dependent RNA polymerase, L protein, Bunyavirales, Cryo-EM, viral replication, suramin, antiviral drug design

INTRODUCTION

Crimean-Congo hemorrhagic fever virus (CCHFV), the causative agent of Crimean-Congo hemorrhagic fever, is an enveloped, negative-sense single-stranded RNA virus (NSV) belonging to the genus *Orthonairovirus* (family *Nairoviridae*) within the order *Bunyavirales*. The disease manifests as an acute infectious syndrome primarily transmitted through *Hyalomma* tick bites, with secondary transmission occurring via contact with infected blood or body fluids[1-3]. Clinical manifestations include high fever, hemorrhagic signs, and hepatic/renal impairment, with case-fatality rates approaching 40%[4-6]. CCHFV is geographically widespread, being endemic in nearly 50 countries across Africa, Europe, Asia and the Middle East[7]. Given its high pathogenicity, epidemic potential, and the expanding geographic range of its tick vector under climate change, the World Health Organization (WHO) has designated CCHFV a priority pathogen requiring urgent countermeasure development[1,8]. Classified as a biosafety level 4 (BSL-4) agent, no approved vaccines or specific antiviral therapies currently exist for CCHFV. Moreover, the accelerating discovery of novel human pathogens within the genus *Orthonairovirus*—including Songling[9], Wetland[10], and Xuecheng[11] viruses—underscores the urgent need to develop effective therapeutic interventions.

The CCHFV genome comprises three RNA segments: the S segment encoding the nucleoprotein (NP), the M segment encoding the glycoprotein precursor (GPC), and the L segment encoding the large RNA-dependent RNA polymerase (RdRp, also referred to as the L protein)[12]. The L protein is a multi-domain and multifunctional enzyme that catalyzes viral RNA replication and transcription, and possesses cap-snatching activity[5,13]. Structural and functional insights have thus far been largely confined to the endonuclease domain[14] and the N-terminal ovarian tumour (OTU)-like domain[15-18], which exhibits deubiquitinating and deISGylating activities that counteract RIG-I-mediated innate immunity. Given its central role in viral replication, the RNA polymerase represents a promising target for antiviral development. Determining the high-resolution structure and mechanistic details of this viral RNA polymerase is therefore crucial for

rational inhibitor design. In recent years, structures of L proteins from several highly pathogenic members of the *Bunyavirales*—including arenaviruses (e.g., Machupo virus [MACV][19-21] and Lassa virus [LASV][19,22]), hantaviruses (e.g., Hantaan virus [HTNV][23-25] and Sin Nombre virus [SNV][26]), peribunyaviruses (e.g., La Crosse virus [LACV][27-29]), phenuiviruses (e.g., severe fever with thrombocytopenia syndrome virus [SFTSV][30-32] and Rift Valley fever virus [RVFV])[33], the plant-infecting tospovirus tomato spotted wilt virus (TSWV)[34]—have been solved, significantly advancing our understanding of replication mechanisms across the order.

However, as a representative member of the family *Nairoviridae*, CCHFV encodes one of the largest known RNA polymerases, containing 3,945 residues with a molecular weight (MW) of approximately 450 kDa—nearly twice the size of typical bunyavirus L proteins. The exceptionally large size of the full-length L protein makes its expression, purification, and structural determination challenging. While recent concurrent structural studies have provided architectural insights into the CCHFV L protein[35,36], our study complements these findings by capturing structural transitions associated with the stepwise initiation pathway and characterizing small-molecule inhibition mechanisms relevant to antiviral development.

Here, we present high-resolution cryo-electron microscopy (cryo-EM) structures of the CCHFV L protein captured across multiple distinct functional and inhibitor-bound states: the apo form (2.59 Å), the 5' vRNA promoter-bound state (2.75 Å), the 5'/3' vRNA dual-promoter complex (2.65 Å), and the suramin-bound complex (2.33 Å). These structures define the architecture of the polymerase core and reveal the coordinated mechanism of viral RNA promoter recognition, as well as a distinct dual-site inhibitory mechanism mediated by suramin. Together with recent structural studies, these findings provide insights into CCHFV replication mechanisms and polymerase inhibition, with implications for antiviral development targeting the CCHFV replication machinery.

RESULTS

Cryo-EM structure of the CCHFV L protein

The full-length CCHFV L protein (3,945 amino acids; ~450 kDa) (Figure 1A) poses a considerable challenge for recombinant expression and purification due to its large size. After evaluating multiple expression strategies, we successfully expressed the full-length protein carrying a C-terminal Twin-Strep tag in mammalian HEK293F cells. Following purification by Strep-Tactin affinity and size-exclusion chromatography (SEC), the protein eluted as a homogeneous, monodisperse peak corresponding to approximately 450 kDa, consistent with SDS-PAGE analysis (Figures S1A and S1B).

Initial attempts to detect RdRp activity using the wild-type protein were compromised by intrinsic endonuclease activity (Figure S1C). To establish a robust assay, we generated an endonuclease-inactivated mutant (K835A/D839A/K842A) to eliminate potential template degradation (Figure S1C). In a fluorescence-based primer-extension assay with a 26-nt 3' vRNA template and a 15-nt 5'-FAM-labeled primer (Figure S1D), the mutant efficiently catalyzed RNA synthesis, generating extension products reaching the expected full-length of 26 nt (Figures S1E and S1F). We found that Mn^{2+} is essential for CCHFV L catalytic activity and robustly drives RNA synthesis, whereas Mg^{2+} failed to effectively activate the RdRp (Figure S1E). Consequently, Mn^{2+} was incorporated into all subsequent cryo-EM sample preparations and served as the sole divalent cation in all subsequent polymerase assays. Further verification of the reconstituted L protein–promoter complex showed that while full-length product synthesis proceeds with substantially lower efficiency under CTP (C) alone (likely via template slippage and mismatch synthesis[37,38]), and CTP/UTP (UC) conditions yield a strong product, the most robust and efficient synthesis is achieved only when all complementary NTPs (UCA or full NTPs) are provided (Figure S1F). These results confirm that the purified CCHFV L protein possesses template-dependent RdRp activity within a dual-promoter framework, establishing a robust assay for subsequent mechanistic and inhibitory studies.

Single-particle cryo-EM analysis of the CCHFV L protein in the apo state yielded a reconstruction at a global resolution of 2.59 Å (Figures 1B and S2). The final atomic model encompasses residues 928–3227; a large internal segment (residues 1901–2222) and several flexible loops remain unresolved (Figure 1C). Previous studies have structurally characterized the N-terminal OTU (residues 1–159)[39,40] and endonuclease (residues 584–927)[14] domains, whereas the C-terminal region (residues 3228–3945) remains poorly understood. Consistent with observations in other bunyavirus L proteins, the N- and C-terminal auxiliary domains are invisible in the apo state, likely becoming ordered only upon specific triggers such as viral RNA promoter or cofactor binding.

Structural architecture and conservation of the CCHFV L polymerase core

The well-resolved core region of the CCHFV L protein adopts the canonical architecture shared across the order *Bunyavirales*, comprising an N-terminal PA-like domain, a central PB1-like domain, and a C-terminal PB2-like domain (Figure 1A). This modular organization is consistent with those observed in both influenza[41-43] and other bunyavirus L proteins[19,27,32,44]. Specifically, the PA-like domain contains the Linker, Arch, vRBL (viral RNA-binding lobe), and Core lobe; the PB1-like domain forms the catalytic core, housing the Fingers, Palm, Thumb subdomains; and the PB2-like domain consists of the Bridge, Thumb ring, and Lid. Structural comparisons reveal strong conservation of this core fold with RNA polymerases from other members of the order *Bunyavirales*, including SFTSV (*Phenuiviridae*)[31,32], LACV (*Peribunyaviridae*)[27], HTNV (*Hantaviridae*)[23-25], as well as LASV and MACV (*Arenaviridae*)[19] (Figure 2A). Within this conserved core, individual functional subdomains share highly similar architectures, although the Core lobe in CCHFV is slightly enlarged (Figures 2B and S3).

These domains collectively organize into a central catalytic cavity that harbors the eight canonical polymerase motifs (A–H) conserved across viral RdRps (Figure 2C), as determined by sequence alignments. In the CCHFV L protein, the Palm domain houses catalytic motifs A–E,

while the Core lobe and Fingers domain contain motifs G, and F/H, respectively. However, in our cryo-EM structure, motif F was structurally unresolvable due to local flexibility, leaving the remaining seven motifs (A–E, G, and H) clearly defined in the map. Motif A (residues 2346–2367) and motif C (residues 2506–2529) are essential for catalysis, containing invariant aspartate-aspartate residues (D2517 and D2518) that coordinate metal ions for phosphodiester bond formation via interactions involving G2357 (Motif A), D2518 (Motif C), and E2575 (Motif E). Motif B (residues 2474–2489) mediates template recognition and nucleotide binding. These motifs, alongside motifs D (residues 2560–2572), E (residues 2573–2583), G (residues 1523–1533), and H (residues 2399–2402), circumscribe the convergence of four specialized tunnels characteristic of bunyavirus L proteins: the template entry and exit, NTP entry, and nascent RNA exit tunnels[44]. Although the Thumb domain lacks the primary catalytic motifs, it serves as a critical structural boundary to position the 3' vRNA template strand within the active site.

The substrate-free structure reveals both ordered and flexible elements that are functionally linked to replication and transcription. A well-ordered loop (residues 2306–2314) occupies a spatial position corresponding to the Prime-and-Realign (PR) loop (Figure 2C). In segmented negative-strand RNA viruses (NSVs), this element is thought to facilitate initiation by stabilizing the nascent terminal complementary dinucleotide before realignment on the template, such as in LACV[29] and HTNV[23] polymerases. Conversely, a region spatially analogous to the "priming loop" (residues 2838–2860)—an element whose functional role in *Bunyavirales* remains to be fully elucidated and may differ from its namesake in influenza[27]—was not resolved in our map. Similarly, the Arch subdomain implicated in promoter binding, and several regions of the vRBL and Fingers domains exhibit conformational flexibility in the absence of RNA substrate. Additionally, a region absent from the density map (residues 1901–2222) is predicted to fold into a compact domain positioned above the core, similar to the pendant domain observed in the LASV and MACV L protein[19].

Collectively, despite substantial variation in full-length sequence and auxiliary domains among *Bunyavirales* RNA polymerases, the catalytic core regions and essential functional motifs are conserved in both fold topology and spatial arrangement. This structural conservation underscores the catalytic core elucidated here as a critical and common framework for RNA synthesis across the order *Bunyavirales*.

The cryo-EM density map of the CCHFV L protein in the apo state supports the assignment of four bound metal ions—two zinc (Zn^{2+}), one manganese (Mn^{2+}), and one magnesium (Mg^{2+}) ions—with surrounding residues exhibiting compatible coordination geometry for each metal type (Figure 2D). The first zinc ion (Zn1) is coordinated by a zinc-finger motif within the vRBL region (C1028/C1031/C1062/C1065), stabilizing a three-helix bundle that corresponds to a single α-helix in the LACV polymerase[27]. The second zinc ion (Zn2) localizes to the interface between the vRBL and Thumb domains (coordinated by H1090/C1294/H1365/E2788) and is inferred to contribute to structural integrity. The catalytic-site ion is assigned as Mn^{2+}, coordinated by acidic residues from conserved motifs A, C and E (G2357/D2518/E2575) (Figure 2D), consistent with the observed Mn^{2+}-dependent polymerase activity and 5 mM Mn^{2+} in buffer. The non-catalytic surface site at the interface of the Core lobe, Thumb, and Thumb ring is modeled as Mg^{2+} (coordinated by R1427/E1430/E3081/N3083) (Figure 2D), supported by CheckMyMetal validation[45] and the ~1,000-fold higher intracellular abundance of Mg^{2+} over Mn^{2+}, supporting Mg^{2+} as the most likely occupant during protein folding.

Structural basis for 5' vRNA promoter recognition

For negative-sense single-stranded RNA viruses, the genomic vRNA must be transcribed into positive-sense mRNA by the viral L protein. This process relies on conserved terminal untranslated regions (UTRs) acting as promoters: the 5′ vRNA end folds into a characteristic "hook" to specifically bind and allosterically prime the inactive polymerase[41,44], whereas the 3′ vRNA end serves as the synthesis template. Preconditioned on this 5′ engagement, they form a

functional 5′/3′ dual-promoter complex that positions the 3′ template within the catalytic core for de novo initiation[27,29]. Given that recognition of the 5' vRNA "hook" constitutes the primary event in orchestrating CCHFV replication, we assembled the CCHFV L protein–promoter complex by incubating the purified protein with chemically synthesized 5' vRNA fragments at a molar ratio of 1:1.2. Subsequent cryo-EM single-particle analysis yielded a reconstruction at an overall resolution of 2.75 Å, where the density for the bound 5' vRNA was sufficiently well-defined to support reliable atomic modeling (Figures 3A, 3B and S4).

Compared with the apo state structure, the 5' vRNA-bound complex reveals additional well-resolved regions, including the vRBL (residues 1104–1155 and 1171–1220) and Fingers domain (residues 2405–2419 and 2432-2446) (Figures 3C, S5A and S5C). The Arch domain (residues 1234–1255), disordered in the apo state, undergoes a clear disorder-to-order transition upon RNA binding (Figure 3B, 3C, S5A, and S5B)—a conformational change also observed in HTNV[23] and TSWV[34]. Structural superposition with the apo structure shows a subtle expansion of the polymerase scaffold (Figure S5D), indicating a slight conformational opening induced by 5' vRNA engagement, with no other large-scale rearrangements observed.

In the CCHFV L–vRNA complex, the first 11 nucleotides of the 5' vRNA promoter are clearly resolved (Figure 3B). The RNA adopts the characteristic hook-like conformation similar among *Bunyavirales* 5' vRNA promoters[22,23,27], with its architecture stabilized primarily by a canonical Watson–Crick base pair between C2 and G8 (Figure 3B). The single-base-pair configuration resembles those observed in SFTSV and LASV RNA polymerases[22,32], but differs from the two-base-pair architectures found in HTNV (G3–C11 and U4–A10) and TSWV (G2–C9 and A3–U8)[23,34]. The 5' vRNA binds within a cleft formed by the Fingers, vRBL, Core lobe and Arch domains (Figures 3A and 3C). This binding pocket exhibits a strong positive electrostatic potential, complementary to the RNA backbone (Figures 3D and S5E). The hook-binding cleft formed by these domains is structurally conserved in other bunyavirus polymerases—including HTNV, LASV and LACV (Figure S5F)—indicating that this architecture mediating 5' vRNA promoter

recognition represents a conserved feature associated with replication initiation across the *Bunyavirales* order.

The 5' vRNA is anchored within the binding pocket through an extensive and specific network of non-covalent interactions (Figures 3E and 3F). Its phosphate backbone is coordinated by salt bridges and hydrogen bonds involving residues from multiple domains: N1077 and K1080 (vRBL), R1252 (Arch), K1261, E1380, Q1517, S1549, R1551, R1552 and N2413 (Core lobe), and N2447 (Fingers). The RNA bases and ribose sugars are further stabilized by hydrogen bonds with S1073, N1381 and Y1399 (vRBL); R1257, N1259 and D1260 (Core lobe); S1248, R1252 and F1255 (Arch); and S2407, K2410, S2443 and N2447 (Fingers). Additionally, three key cation–π interactions lock the RNA in place: R1252 with nucleobase G8, R1257 with A5, and R1551 with C4. This intricate interaction network illustrates how electrostatic, hydrogen-bonding, and aromatic interactions act cooperatively to achieve precise, specific promoter docking.

Although 5' vRNA binding stabilizes the adjacent regions—including the Fingers, vRBL, and Arch domains—the catalytic motif F and the priming loop remain unresolved. In most bunyavirus RNA polymerases, these elements become ordered upon 5' vRNA binding, priming the enzyme for initiation[23,27,34]. Their absence in the CCHFV L–5' vRNA complex points to a more stringent, checkpoint-like activation mechanism. Thus, 5' vRNA binding induces structural organization of the vRBL and Arch, creating a scaffold for subsequent 3' vRNA recruitment, but is insufficient to fully assemble the active center. We propose that the structural ordering of motif F and the priming loop is functionally dependent on the entry and correct positioning of the 3' vRNA template, contributing to structural organization associated with the initiation of viral replication. This mechanism is consistent with a stepwise process for polymerase activation that mirrors an allosteric paradigm widely observed in other viral RNA-dependent RNA polymerases[23,27,34,41].

Structural basis for 3' vRNA recruitment and dual-promoter complex formation

To advance from a single-promoter architecture to the full pre-initiation assembly, we reconstituted the L protein–dual promoter complex by incubating purified CCHFV L with chemically synthesized 5' and 3' vRNA fragments at a molar ratio of 1:1.2:1.2. Extensive cryo-EM single-particle analysis uncovered multiple conformational states within the sample, including two apo-like forms lacking visible vRNA density (designated as apo2 and apo3), a 5' vRNA-bound state (state 2), and the binary 5'/3' vRNA dual-promoter complex (Figure 4, S6 and S7). While apo2 is nearly identical to the ground-state apo conformation, apo3 exhibited significant structural rearrangements despite the absence of bound vRNA (Figures S7A–S7C). Notably, apo3 displayed an ordered vRBL domain and a stabilized Fingers subdomain, closely resembling the "primed" architecture observed in the 5' vRNA-bound state (Figures S7C and S7D). However, the Lid–Bridge region remained disordered in apo3, distinguishing it from both the apo and the 5' vRNA-bound states (Figure S7C). This observation suggests that the CCHFV L protein can transiently sample a promoter-ready conformation even without RNA ligands, potentially facilitating initial viral RNA recruitment. Regarding the 5' vRNA-bound state 2, it differs from the previously described state 1 in that the Arch domain is unresolved and only the first 10 nucleotides of the 5' vRNA are visible, with nucleotide A11 being disordered. In this state, the Lid–Bridge region shows increased stability relative to the apo form.

Comparison with the 5' vRNA-only state reveals that the recruitment of 3' vRNA induces pronounced stabilization throughout the catalytic core, particularly in the vRBL and Bridge regions (Figures 4A, 4D and S8A). Structural elements that remain flexible or unresolved in both the apo and 5' vRNA-bound state 1—including a specific vRBL loop (residues 1094–1103) and a Bridge segment (residues 2865–2868, 2942–2955, 2965–2972, and 2989–2991)—become highly ordered upon 3' vRNA engagement (Figure S8A). While the vRBL exhibits partial ordering in the apo3 and 5' vRNA-bound conformations, it undergoes further stabilization and a concerted inward rotation toward the incoming 3' vRNA, which is tightly coordinated with the disorder-to-order transition of the aforementioned regions (Figure S8B). Together, these movements create a

functional secondary binding channel—a canonical RNA-recruitment track widely conserved among NSVs[19,23,27,28,41]—to accommodate the 3' vRNA template. In this context, the 3' vRNA appears to act as an interfacial tether that electrostatically bridges and stabilizes the vRBL, Bridge, and Thumb ring domains into a compact, functionally competent pre-initiation architecture.

In the dual-promoter complex, nucleotides 19–26 of the 3' vRNA are fully modeled, revealing a clear spatial trajectory through the newly stabilized channel. These nucleotides represent a 3' terminal promoter motif that is highly conserved across the *Orthonairovirus* genus. Notably, the 3' end extends toward the periphery of the protein core and points away from the central catalytic active site. This arrangement, in which the 3' terminus is positioned in a secondary binding site rather than being directly inserted into the catalytic cavity, represents a canonical pre-initiation configuration inherent to NSVs. This conformation is consistent with mechanistic models for segmented NSV polymerases, including influenza viruses and other bunyaviruses, which utilize a homologous secondary binding site to anchor the conserved promoter region prior to replication activation[19,23,27,28,41].

Specifically, these terminal nucleotides are anchored within the channel through an extensive network of interactions, including electrostatic complementarity, hydrogen bonding, and aromatic stacking (Figures 4B and 4C). The negatively charged phosphate backbone is positioned by a prominent positively charged surface patch formed by K1094, K1145, K1217, R1348, and K2954, which establish critical salt bridges (Figure 4C). Binding affinity is further enhanced by an extensive hydrogen-bonding network involving the side chains of K1145, K1217, S1219, R1348, and N1354 with the RNA bases and ribose 2'-OH groups (Figure 4C). Base-specific recognition is provided by R1111 and N1354, while main-chain atoms of K1094, F1096, D1107, K1362, and Y2956 contribute additional stabilizing interactions. Aromatic residues W1214 (in the ordered vRBL loop) and F2957 (in the Bridge) engage in π-stacking with RNA bases, forming a hydrophobic "sandwich", supplemented by van der Waals contacts from F1353 and T1148, and a cation–π interaction from R1111 (Figure 4C). This multifaceted recognition ensures high-affinity

binding and precise spatial positioning of the 3' vRNA template, maintaining its spatial segregation from the active site until subsequent large-scale local conformational rearrangements trigger its release into the catalytic core.

Notably, 3' vRNA binding triggers reciprocal remodeling at the 5' vRNA site (Figure 4D). Nucleotide A11 of the 5' vRNA becomes poorly resolved, correlating with the disordering of the Arch domain (well-defined in the 5' vRNA-only state 1) (Figures 4B and S8A). This dynamic behavior is clearly reflected in the localized cryo-EM map comparison, showing that the 5' vRNA density evolves from a well-resolved hook conformation into a flexible, diffuse state upon transition to state 2 and the dual-promoter complex (Figure S8C). This observation suggests that partial disengagement or increased dynamics of the 5' vRNA hook is required to accommodate the incoming 3' template, representing a structural maturation step toward an initiation-competent conformation. Furthermore, the Lid domain also achieves relative stabilization (Figure S9C).

Dynamic stepwise stabilization and conformational maturation of the viral promoter-binding region

Comparative structural analysis among the apo, 5' vRNA-bound, and 5'/3' vRNA dual-promoter-bound states delineates a stepwise stabilization pathway of the promoter-binding region that emerges from a dynamic equilibrium between conformational states (Figure S9). The CCHFV L protein populates a highly flexible, "open" apo conformation that is stochastically sampled, then transitions into an allosterically primed intermediate upon 5' vRNA binding. In this primed state, the Fingers, vRBL, and Arch domains organize into an ordered platform, with the vRBL likely serving as a key scaffold to facilitate subsequent recruitment and precise positioning of the 3' vRNA. Notably, even in the absence of RNA ligands, a transient ensemble (the apo3 structure) samples a partially pre-stabilized primed conformation, thereby lowering the entropic barrier for initial promoter engagement. Intriguingly, the vRBL remains only weakly ordered and partially resolved across several of these intermediate cryo-EM maps, reflecting that this domain

311 stochastically samples a promoter-ready conformation but retains significant dynamism. Upon
312 assembly of the dual-promoter complex, this conformational fluidity is effectively quenched. The
313 polymerase adopts a compact architecture resembling a functional pre-initiation complex (PIC),
314 characterized by enhanced ordering of the Fingers, vRBL, Bridge, and Lid domains, which
315 collectively enclose the catalytic chamber.

316 In summary, the CCHFV L protein progresses through a conformational maturation process
317 within a dynamic equilibrium: it stochastically samples a highly flexible apo state, transitions to a
318 5' vRNA-primed intermediate, and finally shifts toward a fully stabilized PIC upon 3' vRNA
319 recruitment (Figures 4D and S9). These transitions are inherently reversible, providing multiple
320 regulatory checkpoints that ensure accurate promoter recognition and precise active-site
321 organization before committing to efficient, high-fidelity viral RNA synthesis.

322

323 **Binding and inhibition of the CCHFV L protein by suramin and its derivatives**

324 To identify antiviral lead compounds targeting the CCHFV RNA polymerase, we evaluated
325 suramin and its structural analogues (NF023, NF157, NF449, and NF546) (Figure 5A and S10A-
326 D). Suramin is a recognized broad-spectrum antagonist of viral polymerases across diverse
327 families, including Ebola virus[46], coronaviruses[47] and norovirus[48]. Within the *Bunyavirales* order,
328 suramin has also shown activity against SFTSV and RVFV, albeit primarily through nucleoprotein
329 binding[49,50]. To explore its potential as an optimizable chemical scaffold, we characterized these
330 compounds using primer-extension assays to determine functional enzymatic inhibition.

331 Primer-extension assays confirmed that suramin exerts a potent dose-dependent inhibitory
332 effect on CCHFV L protein RdRp activity, achieving near-complete inhibition at concentrations
333 between 3.9 and 7.8 μM (Figure 5B). Enzymatic assays further revealed that all tested suramin
334 analogues exhibit varying degrees of inhibitory potency. Among them, NF157 retained inhibitory
335 activity comparable to that of suramin, whereas NF449 showed a slightly reduced inhibitory effect.
336 In contrast, the inhibitory activities of NF023 and NF546 are significantly diminished (Figure S10E-

H). Taken together, these results demonstrate that chemical analogues based on the suramin scaffold can effectively suppress the enzymatic function of the CCHFV L protein.

To elucidate the inhibitory mechanism, we determined the cryo-EM structure of the CCHFV L–suramin complex at 2.33 Å (Figures 5C and S11). The density map unexpectedly revealed two spatially distinct binding sites (Site 1 and Site 2) (Figure 5C), characterized by multi-ligand occupancy: two suramin molecules at Site 1 and three at Site 2 (Figure 5D). This unusual dual-site, multi-ligand occupancy suggests a sophisticated inhibitory mechanism that differs from the direct active-channel blocking mediated by individual suramin molecules previously observed in other viral polymerases[46-48], establishing a direct link from biochemical potency to structural visualization.

Specific dual-site inhibitory mechanism of suramin against CCHFV RNA polymerase

Suramin is a symmetrical polyanionic molecule centered on a urea core, with its flanking aromatic rings labeled D through A (and D' to A') from the innermost benzene (D/D') and intermediate methyl-benzene (C/C') to the terminal naphthalene proximal (B/B') and distal (A/A') rings (Figures S12A).

At Site 1, two partially resolved suramin molecules (designated Suramin 1A and 1B, respectively) were identified. Suramin 1A was modeled as a fragment comprising one naphthalene system (rings A and B) and two benzene rings (rings C and D), whereas Suramin 1B includes only rings A–C (Figures 5D and S12B). These two ligand fragments associate as a dimeric unit stabilized via reciprocal π–π stackings (Suramin 1B rings A to Suramin 1A ring C, and Suramin 1B ring C to Suramin 1A ring B), alongside an intramolecular hydrogen bond (Figures 5D and S12B). This dimer engages the L protein through an extensive interface involving π–π interactions—specifically, Y1399 with Suramin 1A ring C and R1552 with Suramin 1A ring B—alongside a dense network of hydrogen bonds and salt bridges (R1403, Q1404, N1514, S1515, Q1516, S1549, R1551, and R1552 with Suramin 1A naphthalene sulfonate groups) (Figures 6A and S12C).

Mechanistically, the suramin dimer at Site 1 occupies the positively charged cleft that serves as the binding pocket for the 5' vRNA promoter (Figure 6B). Its sulfonate groups appear to mimic the RNA phosphate backbone electrostatically, engaging key 5' vRNA-binding determinants, including Y1399, S1549, R1551, and R1552 (Figure 6A). Although suramin interacts exclusively with the Core lobe and Fingers (Figure 6B), it stabilizes the overall L protein fold similarly to 5' vRNA, ordering previously flexible regions in the vRBL and Fingers (Figure 5C). Structural comparison shows that suramin induces a subtle contraction around Site 1, whereas RNA binding promotes slight expansion, consistent with its smaller volume relative to the 5' vRNA hook (Figure S13B). Locally, suramin binding remodels the 1373–1380 loop, which undergoes a significant conformational shift, pulling its hosting loop towards the inhibitor (Figures S13A). Bio-Layer Interferometry (BLI) showed that suramin pre-incubation effectively abolishes high-affinity 5' vRNA binding, suggesting its role as a effective competitive inhibitor of the 5' vRNA binding pocket (Figure 6C).

At Site 2, three suramin molecules (Suramin 2A, Suramin 2B, and Suramin 2C) form a trimeric assembly (Figures 5D and S12B) at the exterior Linker–Fingers interface, distal to the catalytic core (Figures 5C, 5D, and 6D). Among these, Suramin 2A is fully resolved, whereas Suramin 2B is modeled with one naphthalene system (rings A and B) and three benzene rings (rings C, D, and D'), and Suramin 2C comprises the central four benzene rings (rings C/D/C'/D'). Stabilized by ten internal π–π stacks and ten inter-ligand hydrogen bonds (Figure S12B), the trimeric assembly interacts with the L protein via cation–π interactions (R1671 with Suramin 2A ring D and Suramin 2C ring C; and R1659 with Suramin 2A ring C') and an extensive electrostatic network involving K1565, R1659, R1662, N1669, K1672, A1673, S1761, and Q1768 (Figures 6E and S12D), where a positively charged patch anchors the negatively charged suramin assembly (Figure 6F). Suramin binding stabilizes K1672 and A1673 while inducing a forward shift of R1671 and the inward folding of the 1652–1657 loop, mediated by electrostatic interactions between K1655/K1656 and the drug's sulfonate groups (Figures 6E, S12D, and S13C). Given the essential role of the Fingers

389 domain in template translocation, we propose that suramin likely mediates an interfacial
390 conformation-trapping effect at Site 2, potentially restricting the conformational plasticity required
391 for the polymerase cycle and thereby contributing to allosteric inhibition.
392
393 ## DISCUSSION
394 Here, we present high-resolution cryo-EM structures of the CCHFV RNA polymerase catalytic
395 core in multiple functional states. These structures provide structural insights into viral promoter
396 recognition and reveal a distinct dual-site inhibitory mechanism. Our comparative analysis shows
397 that the core of the CCHFV L protein adopts the canonical fold conserved across the order
398 *Bunyavirales*[19,23,27,31,33,44]. Specifically, key subdomains—including the catalytic Palm and Thumb,
399 the active-site motifs, the 5' vRNA-binding pocket, and the 3' vRNA-binding secondary site—
400 exhibit high structural similarity to other bunyavirus polymerases[23,27,31,33], underscoring an
401 evolutionarily conserved catalytic framework.
402 Beyond this conserved scaffold, our findings uncover a highly dynamic promoter assembly
403 process. The polymerase undergoes a stepwise conformational transition from a highly flexible,
404 maximally "open" apo state to a partially ordered 5' vRNA-bound intermediate, and finally to a
405 more compact dual-promoter complex (PIC) (Figure 7A and 7B). This progressive stabilization
406 acts as an evolutionary checkpoint, ensuring that template recruitment occurs only after precise
407 recognition of the 5' vRNA "hook". This "activation-before-loading" mechanism serves as a
408 sophisticated gating mechanism to prevent non-specific transcription in the complex cellular
409 environment. Unlike the largely pre-formed promoter pockets of influenza polymerases[41,42], in
410 which the PA-Arch remains structurally ordered even in the absence of the 5' vRNA “hook”, the
411 CCHFV L protein exhibits pronounced conformational plasticity. The transiently primed apo3 state
412 provides direct evidence for a pre-existing conformational equilibrium, suggesting that the CCHFV
413 polymerases favor an induced-fit activation over a rigid lock-and-key model[51].

Recently, two concurrent studies reported structures of the CCHFV L protein[35,36]. Systematic comparison shows that our apo1/2, 5' vRNA-bound state 1, and dual-promoter complex are nearly identical to the corresponding structures in those studies, with only minor local variations. Key regulatory elements such as motif F and the priming loop remain unresolved across all three works, highlighting their intrinsic flexibility. However, our study provides additional complementary insights by capturing multiple intermediate conformations within the same functional states (apo1/2/3 and 5' vRNA-bound state 1/2). This enables us to propose a more continuous model of the stepwise promoter assembly pathway.

Therapeutic targeting of the bunyavirus polymerase remains a formidable challenge; current research has primarily focused on nucleoside analogs acting as chain terminators, though their clinical efficacy remains a subject of debate[6,52-56]. In contrast, non-nucleoside inhibitors (NNIs) like suramin offer a complementary strategy. Suramin has been reported to inhibit various viral polymerases through distinct mechanisms, such as blocking the NTP entry channel in EBOV[46], occupying the catalytic chamber in SARS-CoV-2[47], or hindering template positioning in Norovirus[48] (Figure S14). Our data demonstrate that suramin inhibits the CCHFV L protein through a dual-site mechanism (Figure 7C). At Site 1, suramin competitively occupies the 5' vRNA-binding pocket by mimicking the electrostatic features of the RNA phosphate backbone, potentially blocking promoter loading and replication initiation. Simultaneously, at Site 2, suramin induces interfacial conformation-trapping at the Finger–Linker interface, restricting inter-domain flexibility associated with the polymerase cycle—a mechanism reminiscent of arenavirus Z protein regulation[20,21]. Consistent with its inherent flexibility, suramin molecules at both sites are partially modeled as core functional fragments. As a large, flexible polyanionic molecule, unbound or un-assembled regions of suramin retain substantial mobility, often resulting in weak or absent cryo-EM density—a phenomenon commonly observed in other viral polymerase–suramin structures[46-48].

Importantly, our structures demonstrate that suramin binds with high specificity rather than nonspecifically to positively charged surfaces. While the CCHFV L protein contains multiple RNA-binding tracks, suramin is observed exclusively at its two specific sites. While a potential suramin binding mode was proposed via computational docking in the aforementioned study[35], our experimental density reveals its *bona fide* binding architecture, which differs substantially from their theoretical model. This dual-site action affects regions involved in initiation and elongation, which could contribute to a broad antiviral effect and impose a high genetic barrier to resistance by requiring concurrent mutations at two conserved sites[57]. A two-pronged strategy has also been recently reported for ribavirin against TSWV[34], in which ribavirin targets the 5' vRNA hook-binding site while interfering with Motif F rearrangement. Despite differences in specific inhibitory details, both studies identify the 5' vRNA hook-binding pocket as a potentially critical functional vulnerability. These findings suggest that this pocket may represent an attractive broad-spectrum target and that dual-site inhibition represents a potential strategy for antiviral design.

We acknowledge that suramin itself possesses suboptimal drug-like properties, including high molecular weight and notably poor cell permeability, which limit its direct clinical application against CCHFV. Nevertheless, it serves as an effective molecular probe and a valuable chemical scaffold for future intervention strategies. As a molecular probe, suramin has enabled us to experimentally map two distinct and druggable "hotspots" on the CCHFV polymerase. This structural mapping provides a framework for the rational design of inhibitors targeting currently uncharacterized functional regions. Furthermore, as a chemical scaffold, the efficacy of suramin analogs in our study supports further optimization of this chemical scaffold to improve binding affinity, membrane permeability, and metabolic stability.

Limitations of this study

While this study provides detailed mechanistic insights into CCHFV polymerase function, several limitations should be noted. First, our high-resolution cryo-EM structures encompass only the

catalytic core region, which represents approximately half of the full-length, ~450 kDa L protein. Therefore, the structural organization and functional roles of the extensive N- and C-terminal auxiliary domains remain uncharacterized in this work, and these regions may contain nairovirus-specific regulatory elements. Second, although suramin successfully mapped druggable inhibitor-binding pockets, its inherent suboptimal drug-like properties restrict its direct clinical usage. Dedicated medicinal chemistry optimization will be required to develop clinically viable inhibitors. Finally, our proposed stepwise initiation stabilization pathway is based on static structural snapshots; future single-molecule biophysical and solution-based biochemical studies will be essential to fully validate and visualize these dynamic transitions in real time. In the future, structural studies of the full-length L protein, combined with chemical optimization and dynamic assays, will be necessary to turn these structural frameworks into effective antiviral therapeutics.

RESOURCE AVAILABILITY

Lead contact

Requests for further information and resources should be directed to and will be fulfilled by the lead contact, Jun Ma (majun@szbl.ac.cn).

Materials availability

All expression plasmids used in this study are available from the lead contact without restriction.

Data and code availability

• The cryo-EM density maps and corresponding atomic coordinates have been deposited in the Electron Microscopy Data Bank (EMDB) and Protein Data Bank (PDB), respectively, under accession codes: CCHFV L protein alone (Apo1): PDB 22TE and EMD-68655; Apo2 state (from dual-promoter dataset): PDB 26KD and EMD-80710; Apo3 state (from dual-promoter dataset): PDB 26KB and EMD-80708; L–5' vRNA complex (State 1): PDB 22TR and EMD-68663; L–5' vRNA complex (State 2, from dual-promoter dataset): PDB 26KA and EMD-80707; L–5'/3' vRNA-bound dual-promoter complex: PDB 26JZ and EMD 80706; L–suramin complex: PDB 22TH and EMD-68657.

• This paper does not report original code.

• All data reported in this paper will be shared by the lead contact upon request.

• Any additional information required to reanalyze the data reported in this paper is available from the lead contact upon request.

ACKNOWLEDGMENTS

Cryo-EM data collection was performed at the Structural Biology Core Facility of Shenzhen Medical Academy of Research and Translation (SMART). We are grateful to Dr. Gang Fu for assistance with TEM maintenance, cryo-EM sample screening, and data collection. We thank the Sample Preparation and Analysis Core Facility of the Bio-Tech Center of SMART for technical support for BLI analysis. This work was supported by grants from the Shenzhen Bay Laboratory Startup Fund (21330061) to J.M.

AUTHOR CONTRIBUTIONS

J. M. conceived and supervised the project, and designed all the experiments. K.Y., H.W. and X.L. performed protein purification and biochemical assays. H.W., X.L. and J.Z. prepared and screened cryo-EM specimens. H.W., Z.L. and J.Z. collected and processed cryo-EM data and built the atomic models. Y.W. supervised the experiments and reviewed the manuscript. J.M. wrote the manuscript with assistance from K.Y. All authors contributed to data analysis, discussed the results and approved the final manuscript.

DECLARATION OF INTERESTS

The authors declare no competing interests.

DECLARATION OF GENERATIVE AI AND AI-ASSISTED TECHNOLOGIES IN THE WRITING PROCESS

No generative AI was used in this work.

SUPPLEMENTAL INFORMATION

Document S1. Figures S1–S14, Tables S1–S2

FIGURE TITLES AND LEGENDS

Figure 1. Cryo-EM structure of the Crimean-Congo hemorrhagic fever virus L protein

(A) Domain architecture of the CCHFV L protein. Domain assignments are based on structural conservation among viral RNA polymerases of the order *Bunyavirales*. Domains are colored as follows: Linker (gray), Core lobe (wheat), vRBL (magenta), Arch (smudge), Fingers (orange), Palm (pink), Thumb (slate), Bridge (red), Thumb ring (cyan) and Lid (green). Residue boundaries are indicated above. Solid bars indicate regions resolved by cryo-EM; gray hatched bars represent known functional domains (OTU and endonuclease) that were not resolved. Structurally and functionally uncharacterized regions are shown in white. Regions corresponding to PA, PB1 and PB2 are indicated.

(B) Cryo-EM density maps of the apo CCHFV L protein shown in three orthogonal views and colored according to the domain scheme in (**A**). Key structural features are labeled.

(C) Cartoon representation of the CCHFV L protein in the same orientations as (**B**), with domains colored accordingly. See also Figures S1 and S2, and Table S1**.**

Figure 2. Structure and conservation of the CCHFV L protein

(A) Structural comparison of the CCHFV L protein (this work) with other polymerases of the order *Bunyavirales*: SFTSV (PDB 8AS7), LACV (PDB 5AMR), HTNV (PDB 8C4T), and LASV (PDB 7OJN). The overall fold is highly conserved across the *Orthonairovirus*, *Bandavirus*, *Orthobunyavirus*, *Orthohantavirus*, and *Mammarenavirus* genera.

(B) Domain-specific structural superposition with SFTSV. Detailed alignment of individual segments (Linker–Fingers, Core lobe, Palm, vRBL, Thumb-Thumb ring-Lid) against SFTSV (PDB 8AS7), highlighting the similarity of secondary structural elements. The CCHFV L protein is color-coded by domain as in (A), whereas SFTSV is rendered as a semi-transparent, light-gray cartoon for contrast.

(C) Conservation of key RdRp catalytic motifs and loops. The arrangement of conserved viral RdRp motifs A–H and the Prime-and-Realign (PR) loop is shown; each motif is colored differently with its amino acid ranges labeled. Motif F and the priming loop were not resolved. Key residues D2517 and D2518 are shown as sticks.

(D) Metal ions identified in the cryo-EM density map. The map reveals four bound metal ions: two zinc (Zn^{2+}), one manganese (Mn^{2+}), and one magnesium (Mg^{2+}) ion. Panels 1 and 2 show two structural Zn^{2+} ions, coordinated by C1028/C1031/C1062/C1065 and H1090/C1294/H1365/E2788, respectively. Panel 3 details the catalytic-site Mn^{2+} ion coordinated by G2357/D2518/E2575, while panel 4 displays the non-catalytic surface Mg^{2+} ion coordinated by R1427/E1430/E3081/N3083. See also Figures S1 and S3**.**

Figure 3. Recognition of the 5' vRNA hook by the CCHFV L protein

(A) Overall view of the CCHFV L protein (colored as in Figure 1) in complex with the 5' vRNA (green). Left, cryo-EM density map; right, atomic model in cartoon representation. The RNA binds in a pocket formed by the vRBL, Arch, Fingers, and Core lobe domains.

(B) Cryo-EM density map (mesh) and atomic model (sticks) of the 5' vRNA, which adopts a characteristic stem-loop "hook" structure formed by base pairing between nucleotides C2-G8.

(C) Close-up view of the 5' vRNA binding pocket. Structural comparison of the 5' vRNA-bound state (left) and the apo state (right) shows that RNA binding induces local conformational stabilization in the Arch, vRBL and Fingers domains.

(D) Electrostatic potential surface of the RNA-binding cleft showing that the 5' vRNA hook binds into a highly basic cavity. Scale bar is shown.

(E) Detailed interaction network recognizing the 5' vRNA. Interacting residues are shown as sticks and labeled; RNA is shown as a cartoon and the protein backbone as a transparent cartoon.

(F) Schematic diagram summarizing the intermolecular contacts between L protein residues and the 5' vRNA nucleotides. Hydrogen bonds and salt bridges are indicated by dashed lines; cation–π interactions by double solid lines. See also Figures S4 and S5, and Table S1**.**

Figure 4. Structural basis of 5' and 3' vRNA recognition by the CCHFV L protein

(A) Overall structures of the CCHFV L–5′/3' vRNA dual-promoter complex. Cryo-EM density map (left) and corresponding atomic model (right) of the CCHFV L protein bound to 5' vRNA (green) and 3' vRNA (yellow). The L protein is colored by domain as in Figure 1. The 5' end of the 3' vRNA is indicated to depict its

canonical trajectory through the secondary binding site, showing that its 3' end is directed away from the central catalytic active site.

(B) Cryo-EM density for bound vRNA. Close-up views of the 5' vRNA (top) and 3' vRNA (bottom) density maps (gray mesh), with the atomic models shown as sticks. The maps are contoured at 2.7σ. Nucleotides are labeled (U1–A10 for 5' vRNA; C19–A26 for 3' vRNA).

(C) Detailed interactions between CCHFV L and 3' vRNA. Left: Detailed view of the 3' vRNA binding pocket. Key residues involved in RNA recognition are shown as sticks, and the RNA is shown in cartoon representation. Right: Schematic representation of the protein–RNA interaction network. Hydrogen bonds and salt bridges are indicated by dashed lines. The π–π interaction (W1214/F2957), cation–π (R1111), and hydrophobic (F1353) interactions are indicated by solid gray lines. Residues are color-coded by their respective domains as in (A). Note that panels (B) and (C) have been reoriented relative to (A) for optimal viewing.

(D) Conformational changes upon 3' vRNA binding. Comparison of the vRBL, Arch, and Bridge domains between the 5' vRNA-bound (left) and the 5'/3' vRNA-bound (right) states, highlighting significant conformational rearrangements. Note the movement of the vRBL domain, stabilization of the Bridge domain, and destabilization of the Arch domain upon recruitment of the 3' vRNA promoter. The 5' and 3' ends of the 3' vRNA are indicated. See also Figures S6–S9 and Table S2**.**

Figure 5. Structural basis for CCHFV L protein inhibition by suramin

(A) Chemical structure of suramin. Suramin is a symmetrical polyanionic compound featuring multiple sulfonate groups.

(B) Dose-dependent inhibition of CCHFV L polymerase activity by suramin. Representative *in vitro* primer-extension assays demonstrate that suramin potently inhibits RdRp activity, with near-complete suppression of the product observed at concentrations ranging from 3.9 to 7.8 μM. Data are representative of three independent experiments.

(C) Overall structures of the CCHFV L–suramin complex. Cryo-EM density map (left) and corresponding atomic model (right) of the CCHFV L protein bound to suramin at two distinct sites. The L protein is colored

by domain as in Figure 1. Suramin clusters are designated as Suramin 1 (Site 1, dark green) and Suramin 2 (Site 2, coral).

(D–E) Cryo-EM density for bound suramin clusters. Close-up views of the density maps (gray mesh) for Suramin 1 (D) and Suramin 2 (E), with the molecular models shown as sticks. Suramin 1 comprises a dimeric unit (Suramin 1A in green and 1B in cyan) with its map contoured at 5.0 σ. Suramin 2 anchors a trimeric assembly (Suramin 2A in magenta, 2B in salmon, and 2C in red) with its map contoured at 3.0 σ. For clarity, the overall clusters and their individual disassembled components are displayed alongside each other; the chemical rings (labeled A–D and A'–D') and their corresponding local density support are explicitly marked in the separate views on the right. See also Figures S10 and S11, and Table S1**.**

Figure 6. Dual-site inhibitory mechanism of suramin against the CCHFV L protein

(A) Detailed interaction network at Site 1. The suramin dimer forms an extensive network of interactions within the vRBL and Core lobe, mimicking the electrostatic properties used for 5' vRNA recognition.

(B) Structural comparison of the 5' vRNA-binding pocket. Left: Close-up of the Site 1 with Suramin 1 occupying the pocket. Right: Superposition with the 5' vRNA-bound state (protein in cartoon, RNA in green cartoon, suramin in cyan sticks), highlighting the steric clash between suramin and the 5' vRNA hook.

(C) Competitive inhibition of 5' vRNA binding by suramin. Bio-Layer Interferometry (BLI) sensorgrams show that pre-incubation with suramin (0–8 μM) leads to a dose-dependent reduction in L protein binding to immobilized vRNA.

(D) Conformational remodeling of the Fingers–Linker interface. Comparison between the suramin-bound (top) and apo (bottom) states reveals that suramin binding induces ordering and conformational shifts of the Fingers loops.

(E) Detailed interactions at Site 2. The trimeric assembly engages residues from the Fingers and Linker domains; the gray surface indicates the ligand-binding cavity. In (**C**) and (**F**), interacting side chains are shown as sticks colored as in (**A**) and suramin molecules are shown as sticks colored as in Figure 5D; hydrogen bonds and salt bridges are indicated by short dashed lines, and cation–π interactions by long dashed lines.

(F) Electrostatic surface representation of Site 2. A positively charged surface complements the assembly of the suramin trimer, which is rich in negatively charged sulfonate groups. See also Figures S12–S14**.**

Figure 7. Proposed model for CCHFV L protein promoter recognition and suramin-mediated inhibition

(A) The resting state of the CCHFV L protein. In the apo form, the polymerase exhibits pronounced dynamic plasticity. Several functional domains and regions, including the vRBL, Fingers, Bridge and Lid (indicated by hatched patterns), are intrinsically flexible or disordered. The catalytic center (red star), various entry/exit tunnels (NTP, template, and product), and the binding pockets for 5' vRNA hook pocket and 3' vRNA secondary binding site are highlighted.

(B) Formation of the pre-initiation dual-promoter complex. Recruitment of the 5' vRNA hook (green) and 3' vRNA template (yellow) drives the stepwise stabilization of the L protein. The 5' vRNA binding first primes the core, followed by 3' vRNA engagement, which functions as an interfacial tether to bridge and stabilize the vRBL and Bridge, and Lid. This conformational transition culminates in the assembly of a compact, functionally competent catalytic chamber, characterized by the ordering of previously flexible regions (now shown as solid colors).

(C) Mechanism of dual-site inhibition by suramin. Suramin suppresses CCHFV L activity through two distinct modes of action: 1) Steric blockade at Site 1 (SVR1): A suramin dimer occupies the 5' vRNA hook-binding pocket, electrostatically mimicking the RNA backbone and competitively blocking 5' vRNA recruitment. 2) Allosteric locking at Site 2 (SVR2): A suramin trimer anchors at the exterior Fingers–Linker interface, acting as an allosteric "lock" (symbolized by the padlock) that restricts the conformational plasticity and domain movements required for the polymerase catalytic cycle. See also Figures S7, S9, S13 and S14**.**

STAR★METHODS

KEY RESOURCES TABLE

REAGENT OR RESOURCE	SOURCE	IDENTIFIER
Bacterial and virus strains		
E. coli Top10	Biomed	Cat# BC101-01
Chemicals, peptides, and recombinant proteins		
$MgCl_2$	Sangon Biotech	Cat# M8266
$MnCl_2$	Sangon Biotech	Cat# A500331
Tween-20	Sigma-Aldrich	Cat# 93773
NTP	Beyotime	Cat# D7383
PEI	Yeasen	Cat# 40816ES03
SMM 293-TII Expression Medium	Sino Biological	Cat# M293TII
D-Biotin	Sangon Biotech	Cat# A600078
Strep-TactinXT 4Flow high-capacity resin	IBA Lifesciences	Cat# 2-5030
Amicon Ultra centrifugal filter (100 kDa)	Millipore	Cat# UFC910008
Superose™ 6 Increase 10/300 GL	Cytiva	Cat# 29148721
Suramin	MedChemExpress	Cat# HY-B0879A
NF023	MedChemExpress	Cat# HY-108676
NF157	MedChemExpress	Cat# HY-108672
NF449	MedChemExpress	Cat# HY-112461
NF546	MedChemExpress	Cat# HY-108661
Deposited data		
Cryo-EM structure of CCHFV L protein alone (Apo1)	This work	PDB: 22TE, EMD-68655
Cryo-EM structure of Apo2 state (from dual-promoter dataset)	This work	PDB: 26KD, EMD-80710
Cryo-EM structure of Apo3 state (from dual-promoter dataset)	This work	PDB: 26KB, EMD-80708
Cryo-EM structure of L–5′ vRNA complex (State 1)	This work	PDB: 22TR, EMD-68663
Cryo-EM structure of L–5′ vRNA complex (State 2 from dual-promoter dataset)	This work	PDB: 26KA, EMD-80707
Cryo-EM structure of L–5′/3′ vRNA-bound dual-promoter complex	This work	PDB: 26JZ, EMD-80706
Cryo-EM structure of L–suramin complex	This work	PDB: 22TH, EMD-68657
CCHFV (strain IbAr10200) genome sequence	GenBank	GenBank: KY484041.1
Experimental models: Cell lines		
HEK293F	Invitrogen	Cat# K900001
Oligonucleotides		
3′ vRNA (26-nt): 5′-UAACGGGGGGAUUGAUAUCUUUGAGA-3′	This work	N/A
5′ vRNA (15-nt): 5′-FAM-UCUCAAAGAUAUCAA-3′	This work	N/A
5′-Biotinylated 5′ vRNA: 5′-Bio-UCUCAAAGAUAUCAA-3′	This work	N/A
5′ vRNA endonuclease substrate (50-nt) : 5′-FAM-UCUCAAAGAUAUCAAUCCCCCCGUUACCCACAUUAAUACAGAGAGCUCCA-3′	This work	N/A
Recombinant DNA		
pCAGGS-CCHFV-L-twin-Strep (wild-type)	This work	N/A
pCAGGS-CCHFV-L-twin-Strep (K835A/D839A/K842A)	This work	N/A
Software and algorithms		

UCSF ChimeraX v1.9	Goddard et al.[58] 2021	RRID:SCR_015872; https://www.cgl.ucsf.edu/chimerax/
PyMOL v2.5.5	Schrödinger, LLC.	RRID:SCR_000305; https://www.pymol.org/
cryoSPARC v4.7.0	Punjani et al.[59] 2017	RRID:SCR_016501; https://cryosparc.com/
EPU v3.12	Thermo Fisher Scientific	N/A
Coot v0.9	Casanal et al.[60] 2020	RRID:SCR_014222; https://www2.mrc-lmb.cam.ac.uk/personal/pemsley/coot/
Phenix v1.20.1-4487	Liebschner et al.[61] 2018	RRID:SCR_014224; https://www.phenix-online.org/
AlphaFold Server	Abramson et al.[62] 2024	RRID:SCR_025885; https://alphafoldserver.com/
ForteBio Data Analysis Software v12.0	Sartorius	https://www.sartorius.com/
GraphPad Prism 9.5	Prism Software	RRID:SCR_002798; https://www.graphpad.com/
Biacore 8k+ evaluation software	Cytiva	https://www.cytivalifesciences.com/
Other		
Quantifoil R1.2/1.3 300 mesh, Au	Electron Microscopy Sciences	Cat# Q325AR1.3
Vitrobot Mark IV system	Thermo Fisher Scientific	RRID:SCR_025773
Cryo Transmission Electron microscope	Thermo Fisher Scientific	Titan Krios G4
Octet RED384 instrument	Sartorius	N/A
Octet Streptavidin (SA) Biosensor	Sartorius	Cat# 18-5019
Biacore 8K$^+$ SPR System	Cytiva	N/A
ChemiDoc MP Imaging System	Bio-Rad	RRID:SCR_019037
96-well black plates	Greiner	Cat# 07-000-110
Series S CM5 sensor chip	Cytiva	Cat# BR100530

EXPERIMENTAL MODEL AND STUDY PARTICIPANT DETAILS

Cell lines

HEK293F cells (originally purchased from Invitrogen) were used for recombinant protein expression. The cells were maintained in SMM 293-TII medium (Sino Biological) at 37 °C with 5% CO_2 in an orbital shaking incubator at 120 rpm. Cells were tested to be mycoplasma-free and seeded at a density of 0.8×10^6 cells/ml for transfection.

METHOD DETAILS

Protein expression and purification

The gene encoding the full-length Crimean–Congo hemorrhagic fever virus (CCHFV) L protein (UniProt: Q6TQR6) was codon-optimized for mammalian cell expression, synthesized, and cloned into the pCAGGS vector with a C-terminal twin-Strep tag. The endonuclease mutant (K835A/D839A/K842A) was generated

667 by site-directed mutagenesis to abolish its cleavage activity for use in *in vitro* RNA polymerase activity
668 assays. Its expression and purification followed the same procedures as described for the wild-type protein.
669 For protein expression, HEK293F (Invitrogen) cells were seeded at a density of 0.8 × 10^6 cells per ml, which
670 were maintained in SMM 293-TII medium (Sino Biological) at 37 °C with 5% CO_2 in an orbital shaking
671 incubator at 120 rpm. A total of 1 mg plasmid and 3 mg polyethylenimine (PEI; Yeasen) were incubated in
672 50 ml fresh medium for 20 min before addition to 1 L of culture. After 24 h, sodium butyrate was added to
673 a final concentration of 5 mM, and cells were incubated for a further 48 h before harvesting by centrifugation
674 (2,500 × *g*, 15 min). Cell pellets were resuspended in Lysis Buffer (50 mM Tris-HCl, pH 8.0, 500 mM NaCl,
675 5% glycerol, 1mM TCEP) supplemented with cOmplete EDTA-free Protease Inhibitor Cocktail (Roche) and
676 lysed by sonication on ice, and the lysate was clarified by centrifugation (22,000 × *g*, 45 min, 4 °C). The
677 supernatant was incubated with Strep-Tactin XT 4Flow resin (IBA Lifesciences) for 60 min at 4 °C. The
678 resin was washed extensively with Wash Buffer (50 mM Tris-HCl, pH 8.0, 500 mM NaCl, 5% glycerol, 1
679 mM TCEP, 1 mM EDTA), and target protein was eluted in the same buffer containing 50 mM D-biotin. The
680 eluted protein was concentrated (AmiconUltra, 100 kDa molecular mass cut-off, Millipore) and further
681 purified by size-exclusion chromatography (SEC) on a Superose 6 Increase 10/300 GL column (Cytiva)
682 equilibrated in Lysis Buffer. Fractions containing the target protein were pooled, concentrated to 2–3 mg/ml,
683 flash-frozen as aliquots in liquid nitrogen, and stored at −80 °C for subsequent biochemical assays. Freshly
684 purified samples were immediately used for cryo-EM sample preparation. Samples from each purification
685 step were analyzed by SDS-PAGE (Figure S1), and protein concentration measured by the absorbance at
686 280 nm using a NanoDrop spectrophotometer (Thermo Fisher Scientific).
687
688 **Cryo-EM grid preparation and data collection**
689 Cryo-EM grids were prepared at 4 °C and 100% humidity using a Vitrobot Mark IV (Thermo Fisher Scientific).
690 A 3 μL aliquot of each sample at a final concentration of 0.7 mg/mL was applied to a freshly glow-discharged
691 Quantifoil R1.2/1.3 300-mesh gold grid. The apo CCHFV L sample was used directly. For the CCHFV L–
692 suramin complex, the protein was pre-incubated with 0.1 mM suramin for at least 30 min on ice before grid
693 application. For the CCHFV L–5' vRNA complex, purified L protein was incubated with 15-nt 5' vRNA
694 promoter (5'-UCUCAAAGAUAUCAA-3') at a molar ratio of 1:1.2 for 10 min on ice immediately before grid

preparation. For the CCHFV L–dual-promoter complex, purified L protein was incubated with 15-nt 5' vRNA and 25-nt 3' vRNA (5'-UAACGGGGGGAUUGAUAUCUUUGAGA-3') promoters at a molar ratio of 1:1.2:1.2 for 30 min and further purified by size-exclusion chromatography. After 10 s of incubation, excess solution was blotted for 3 s (blot force 2) and the grid was plunge-frozen in liquid ethane. Prepared grids were loaded onto a 300 kV Titan Krios microscope (Thermo Fisher Scientific) equipped with a Falcon 4 direct electron detector (Thermo Fisher Scientific). Movies were automatically collected using EPU software (Thermo Fisher Scientific) in super-resolution mode at a nominal magnification of 165,000× (calibrated pixel size = 0.73 Å), with a defocus range of −0.8 to −2.5 µm. Each movie was exposed for 3.4 s with a total exposure dose of ~50 e^{-} $Å^{-2}$. Final datasets consisted of 7,939 (apo CCHFV L protein), 4,848 (L–5' vRNA complex), 6,010 (L–5'/3' vRNA dual-promoter complex), and 5,547 (L–suramin complex) micrographs.

Cryo-EM data processing and reconstitution

All cryo-EM data processing was performed using cryoSPARC v4.7.0[59]. Beam-induced motion was corrected using Patch Motion Correction, and contrast transfer function (CTF) parameters were estimated via Patch CTF Estimation.

For the apo CCHFV L dataset, a total of 3,444,016 particles were automatically picked from 7,939 micrographs. After two rounds of 2D classification, 196,081 particles displaying distinct structural features were selected for *ab initio* reconstruction (using five classes) and subsequent heterogeneous refinement. A final subset of 48,496 particles exhibiting well-defined density was then subjected to local CTF refinement and non-uniform refinement, yielding a 2.59 Å map.

For the CCHFV L–5' vRNA complex dataset, 1,681,455 (Blob picker) and 4,033,305 (Template picker) particles were extracted from 4,848 micrographs. Following two rounds of 2D classification and duplicate removal, 294,558 particles were processed via heterogeneous refinement and 3D classification. A subset of 66,103 particles, representing the best-defined class, underwent reference-based motion correction and non-uniform refinement, resulting in a 2.75 Å reconstruction.

For the CCHFV L–dual-promoter dataset, 3,526,857 (Blob picker) and 1,172,889 (Template picker) particles were picked from 6,010 micrographs. Following two rounds of 2D classification, 190,783 and 52,826 particles were retained, respectively. After duplicate removal, 222,953 particles were subjected to

heterogeneous refinement. The major class (77.1%) was further partitioned into five states via 3D classification. Global CTF refinement and non-uniform refinement yielded high-resolution maps for key states: Apo2 state (37,247 particles, 2.64 Å), Apo3 state (33,001 particles, 2.76 Å), 5'/3' vRNA-bound dual-promoter complex (36,896 particles, 2.65 Å), and 5' vRNA-bound state 2 (33,620 particles, 3.06 Å).

For the CCHFV L–suramin complex, 1,108,952 (Topaz picker) and 3,217,362 (Template picker) particles were picked from 5,547 micrographs. Following two rounds of 2D classification, 384,033 and 402,531 particles were retained, respectively. After merging and removing duplicate particles, 643,772 particles were used for heterogeneous refinement and 3D classification. A final set of 84,039 particles was then subjected to local motion correction, local CTF refinement, and non-uniform refinement, yielding a final map at 2.33 Å.

Global resolutions were determined using the gold-standard Fourier shell correlation (FSC) criterion of 0.143. Local resolution estimation performed within cryoSPARC. Detailed processing workflows and data collection statistics are summarized in Figures S2, S4, S6, and S11; Table S1 and S2.

Atomic model building

Model building was initiated with the CCHFV L–5' vRNA complex. An initial atomic model was generated by segmenting the AlphaFold-predicted model into individual domains and docking them into the cryo-EM density map using UCSF ChimeraX[58]. The model was then subjected to iterative cycles of manual adjustment in Coot[60] and real-space refinement in PHENIX[61] until the model parameters converged, and model geometry and fit met standard validation criteria (including MolProbity score, rotamer and Ramachandran outliers). The models for the apo CCHFV L and the CCHFV L–suramin complex were obtained by rigid-body docking of the refined L–5' vRNA model into their respective cryo-EM maps in UCSF ChimeraX, followed by manual adjustment in Coot. These models subsequently underwent the same iterative refinement protocol as described above. Model statistics are summarized in Table S1 and S2. Structural analysis, model building, and figure preparation were performed using Coot, UCSF ChimeraX and PyMOL (https://pymol.org/).

In vitro RNA polymerase activity assay and inhibition assays

To reconstitute the functional viral promoter, RNA oligonucleotides corresponding to the CCHFV genomic termini were chemically synthesized: a 26-nt 3' vRNA template strand (5'-UAACGGGGGGAUUGAUAUCUUUGAGA-3') and a 5'-FAM-labeled 15-nt 5' vRNA strand (5'-FAM-UCUCAAAGAUAUCAA-3') simultaneously serving as both the primer and the hook. These sequences are derived strictly from the highly conserved terminal regions of the CCHFV genome (strain IbAr10200, GenBank KY484041.1). The 5' vRNA corresponds to the genomic 5' terminus and the 3' vRNA corresponds to the genomic 3' terminus. The 5' vRNA sequence was engineered to optimize base-pairing with the 3' template for enhanced RNA synthesis efficiency. The 3' vRNA template was hybridized with the 5' vRNA at a 1:1.5 molar ratio in Annealing Buffer (50 mM Tris-HCl, pH 8.0, 150 mM NaCl) by heating to 90 °C for 2 min, followed by gradual cooling to 4 °C over 2 h. Standard polymerase reactions (10 μL final volume) were carried out in Reaction Buffer (50 mM Tris-HCl, pH 8.0, 150 mM NaCl, 1 mM DTT, 5% (v/v) glycerol, and 5 mM $MnCl_2$). For divalent cation dependence experiments, $MnCl_2$ was substituted with 5 mM $MgCl_2$ where indicated. Purified CCHFV L protein (0.5 μM) was pre-incubated with 200 nM of the annealed RNA promoter for 10 min on ice. Reactions were initiated by the addition of NTPs to a final concentration of 1 mM each and incubated at 30 °C for 2 h. For dose-dependent inhibition assays, suramin and its derivatives (NF023, NF157, NF449, and NF546) were dissolved in dimethyl sulfoxide (DMSO) to prepare stock solutions. The compounds were serially diluted two-fold in Reaction Buffer to generate a final concentration gradient within the reaction mixtures ranging from 2.0 μM to 125 μM (specifically: 0, 2.0, 3.9, 7.8, 15.6, 31.3, 62.5, and 125 μM) in the presence of 5 mM $MnCl_2$. Purified L protein (0.5 μM) was mixed with the indicated concentrations of each inhibitor and the annealed RNA promoter (200 nM) on ice for 20 min to allow equilibrium binding prior to NTP addition. All reactions were terminated by adding an equal volume of Stop Buffer (20 mM EDTA, 0.01% bromophenol blue, 0.01% xylene cyanol) and heating at 95 °C for 5 min. Extension products were resolved on a 15% denaturing urea–PAGE (7 M urea) at 180 V for 80 min and visualized using a ChemiDoc MP Imaging System (Bio-Rad). All assays were independently repeated at least three times.

In vitro endonuclease activity assay

To characterize the intrinsic endonuclease activity of the wild-type (WT) CCHFV L protein and confirm its inactivation in the endonuclease-defective mutant (K835A/D839A/K842A), an *in vitro* RNA cleavage assay

779 was performed. Purified WT or mutant CCHFV L protein (0.5 μM) was incubated with a 50-nt 5'-FAM-labeled
780 single-stranded RNA (ssRNA) substrate (5'-FAM-
781 UCUCAAAGAUAUCAAUCCCCCCGUUACCCACAUUAAUACAGAGAGCUCCA-3') in the same Reaction
782 Buffer described above. The cleavage reactions were carried out at 30 °C for 1 h, and subsequently
783 terminated and analyzed via denaturing urea-PAGE and imaging under identical conditions as the
784 polymerase assay. All assays were independently repeated at least three times.
785
786 **Bio-layer interferometry (BLI) assay**
787 The binding kinetics between the CCHFV L protein and RNA, along with suramin-mediated competitive
788 binding, were analyzed by bio-layer interferometry on an Octet Red 384 system (Sartorius) at 25 °C with
789 shaking at 1,000 rpm. Streptavidin (SA) biosensors (Sartorius, Cat. # 18-5019) were equilibrated in kinetics
790 buffer (50 mM Tris-HCl, pH 8.0, 100 mM NaCl, 0.05% Tween-20) for 10 min. 200 nM 5'-biotinylated 5' vRNA
791 (5'-Bio-UCUCAAAGAUAUCAA-3') was immobilized on the sensors for 90 s, followed by a 60 s baseline
792 equilibration. For binding kinetics, sensors were incubated with serially diluted CCHFV L protein at
793 concentrations ranging from 200 nM to 3.125 nM (two-fold serial dilutions) for 600 s (association) and then
794 transferred to kinetics buffer for 600 s (dissociation). For the suramin competitive binding assay, 200 nM
795 protein was first pre-incubated with different concentrations of suramin (0.5, 1, 2, 4, 8 μM) at room
796 temperature for 30 min. Protein without suramin served as the control. Parallel reference wells containing
797 immobilized RNA exposed only to 10 μM suramin were used to correct for system drift and non-specific
798 binding. Data were processed using Octet Analysis Studio software to evaluate the competitive binding
799 effect of suramin on the CCHFV-L protein–RNA interaction. All assays were independently repeated at least
800 three times.
801
802 **QUANTIFICATION AND STATISTICAL ANALYSIS**
803 Resolutions of all cryo-EM density maps were determined by the gold-standard FSC = 0.143 criterion, and
804 local resolutions were estimated in cryoSPARC. Atomic models were comprehensively validated using
805 MolProbity. All enzymatic assays were performed in at least three independent experiments, with each run
806 representing a distinct biological replicate yielding reproducible results. Data shown in Figure 1F represent

807 the quantification of signal intensity from three independent replicates. Bar graphs show the mean ± SD,
808 and individual data points are displayed as dots. No data were excluded from the statistical analysis.
809
810 **SUPPLEMENTAL INFORMATION**
811 Document S1. Figures S1–S14, Table S1–S2
812

REFERENCES

1. McFadden, E., Monticelli, S.R., Wang, A., Ramamohan, A.R., Batchelor, T.G., Kuehne, A.I., Bakken, R.R., Tse, A.L., Chandran, K., Herbert, A.S., and McLellan, J.S. (2025). Engineering and structures of Crimean-Congo hemorrhagic fever virus glycoprotein complexes. Cell *188*, 303–315 e313. 10.1016/j.cell.2024.11.008.
2. Ritter, M., Canus, L., Gautam, A., Vallet, T., Zhong, L., Lalande, A., Boson, B., Gandhi, A., Bodoirat, S., Burlaud-Gaillard, J., et al. (2024). The low-density lipoprotein receptor and apolipoprotein E associated with CCHFV particles mediate CCHFV entry into cells. Nat Commun *15*, 4542. 10.1038/s41467-024-48989-5.
3. Monteil, V.M., Wright, S.C., Dyczynski, M., Kellner, M.J., Appelberg, S., Platzer, S.W., Ibrahim, A., Kwon, H., Pittarokoilis, I., Mirandola, M., et al. (2024). Crimean-Congo haemorrhagic fever virus uses LDLR to bind and enter host cells. Nat Microbiol *9*, 1499–1512. 10.1038/s41564-024-01672-3.
4. Golden, J.W., Shoemaker, C.J., Lindquist, M.E., Zeng, X., Daye, S.P., Williams, J.A., Liu, J., Coffin, K.M., Olschner, S., Flusin, O., et al. (2019). GP38-targeting monoclonal antibodies protect adult mice against lethal Crimean-Congo hemorrhagic fever virus infection. Sci Adv *5*, eaaw9535. 10.1126/sciadv.aaw9535.
5. Hawman, D.W., and Feldmann, H. (2023). Crimean-Congo haemorrhagic fever virus. Nat Rev Microbiol *21*, 463–477. 10.1038/s41579-023-00871-9.
6. Frank, M.G., Weaver, G., Raabe, V., State of the Clinical Science Working Group of the National Emerging Pathogens, T., Education Center's Special Pathogens Research, N., and State of the Clinical Science Working Group of the National Emerging Pathogens Training Education Center's Special Pathogens Research, N. (2024). Crimean-Congo Hemorrhagic Fever Virus for Clinicians-Diagnosis, Clinical Management, and Therapeutics. Emerg Infect Dis *30*, 864–873. 10.3201/eid3005.231648.
7. Bente, D.A., Forrester, N.L., Watts, D.M., McAuley, A.J., Whitehouse, C.A., and Bray, M. (2013). Crimean-Congo hemorrhagic fever: history, epidemiology, pathogenesis, clinical syndrome and genetic diversity. Antiviral Res *100*, 159–189. 10.1016/j.antiviral.2013.07.006.
8. WHO (2018). 2018 Annual review of diseases prioritized under the Research and Development Blueprint. World Health Organization Geneva, Switzerland.
9. Ma, J., Lv, X.L., Zhang, X., Han, S.Z., Wang, Z.D., Li, L., Sun, H.T., Ma, L.X., Cheng, Z.L., Shao, J.W., et al. (2021). Identification of a new orthonairovirus associated with human febrile illness in China. Nat Med *27*, 434–439. 10.1038/s41591-020-01228-y.
10. Zhang, X.A., Ma, Y.D., Zhang, Y.F., Hu, Z.Y., Zhang, J.T., Han, S., Wang, G., Li, S., Wang, X., Tang, F., et al. (2024). A New Orthonairovirus Associated with Human Febrile Illness. N Engl J Med *391*, 821–831. 10.1056/NEJMoa2313722.
11. Zhang, M.Z., Bian, C., Ye, R.Z., Cui, X.M., Chu, Y.L., Yao, N.N., Xu, X.W., Ye, J.L., Chen, L., Yang, J.H., et al. (2025). Human Infection with a Novel Tickborne Orthonairovirus Species in China. N Engl J Med *392*, 200–202. 10.1056/NEJMc2410853.
12. Iglesias-Rivas, P., Gonzalez-Vazquez, L.D., and Arenas, M. (2025). Molecular Evolution and Phylogeography of the Crimean-Congo Hemorrhagic Fever Virus. Viruses *17*. 10.3390/v17081054.
13. Zivcec, M., Scholte, F.E., Spiropoulou, C.F., Spengler, J.R., and Bergeron, E. (2016). Molecular Insights into Crimean-Congo Hemorrhagic Fever Virus. Viruses *8*, 106. 10.3390/v8040106.
14. Kuang, W., Tian, Z., Zhang, G., Wu, F., Li, J., Tang, J., Zhang, H., Zhuo, X., Hu, Z., Wang, M., et al. (2026). Structure and function of the nairovirus cap-snatching endonuclease. Nucleic Acids Res *54*. 10.1093/nar/gkaf1515.
15. Leventhal, S.S., Bisom, T., Clift, D., Rao, D., Meade-White, K., Shaia, C., Murray, J., Mihalakakos, E.A., Hinkley, T., Reynolds, S.J., et al. (2024). Antibodies targeting the Crimean-Congo Hemorrhagic Fever Virus nucleoprotein protect via TRIM21. Nat Commun *15*, 9236. 10.1038/s41467-024-53362-7.
16. Akutsu, M., Ye, Y., Virdee, S., Chin, J.W., and Komander, D. (2011). Molecular basis for ubiquitin and ISG15 cross-reactivity in viral ovarian tumor domains. Proc Natl Acad Sci U S A *108*, 2228–2233. 10.1073/pnas.1015287108.

17. Spengler, J.R., Patel, J.R., Chakrabarti, A.K., Zivcec, M., Garcia-Sastre, A., Spiropoulou, C.F., and Bergeron, E. (2015). RIG-I Mediates an Antiviral Response to Crimean-Congo Hemorrhagic Fever Virus. J Virol *89*, 10219–10229. 10.1128/JVI.01643-15.
18. Scholte, F.E.M., Zivcec, M., Dzimianski, J.V., Deaton, M.K., Spengler, J.R., Welch, S.R., Nichol, S.T., Pegan, S.D., Spiropoulou, C.F., and Bergeron, E. (2017). Crimean-Congo Hemorrhagic Fever Virus Suppresses Innate Immune Responses via a Ubiquitin and ISG15 Specific Protease. Cell Rep *20*, 2396–2407. 10.1016/j.celrep.2017.08.040.
19. Peng, R., Xu, X., Jing, J., Wang, M., Peng, Q., Liu, S., Wu, Y., Bao, X., Wang, P., Qi, J., et al. (2020). Structural insight into arenavirus replication machinery. Nature *579*, 615–619. 10.1038/s41586-020-2114-2.
20. Xu, X., Peng, R., Peng, Q., Wang, M., Xu, Y., Liu, S., Tian, X., Deng, H., Tong, Y., Hu, X., et al. (2021). Cryo-EM structures of Lassa and Machupo virus polymerases complexed with cognate regulatory Z proteins identify targets for antivirals. Nat Microbiol *6*, 921–931. 10.1038/s41564-021-00916-w.
21. Ma, J., Zhang, S., and Zhang, X. (2021). Structure of Machupo virus polymerase in complex with matrix protein Z. Nat Commun *12*, 6163. 10.1038/s41467-021-26432-3.
22. Kouba, T., Vogel, D., Thorkelsson, S.R., Quemin, E.R.J., Williams, H.M., Milewski, M., Busch, C., Gunther, S., Grunewald, K., Rosenthal, M., and Cusack, S. (2021). Conformational changes in Lassa virus L protein associated with promoter binding and RNA synthesis activity. Nat Commun *12*, 7018. 10.1038/s41467-021-27305-5.
23. Durieux Trouilleton, Q., Barata-Garcia, S., Arragain, B., Reguera, J., and Malet, H. (2023). Structures of active Hantaan virus polymerase uncover the mechanisms of Hantaviridae genome replication. Nat Commun *14*, 2954. 10.1038/s41467-023-38555-w.
24. Durieux Trouilleton, Q., Housset, D., Tarillon, P., Arragain, B., and Malet, H. (2024). Structural characterization of the oligomerization of full-length Hantaan virus polymerase into symmetric dimers and hexamers. Nat Commun *15*, 2256. 10.1038/s41467-024-46601-4.
25. Keown, J.R., Carrique, L., Nilsson-Payant, B.E., Fodor, E., and Grimes, J.M. (2024). Structural characterization of the full-length Hantaan virus polymerase. PLoS Pathog *20*, e1012781. 10.1371/journal.ppat.1012781.
26. Meier, K., Thorkelsson, S.R., Durieux Trouilleton, Q., Vogel, D., Yu, D., Kosinski, J., Cusack, S., Malet, H., Grunewald, K., Quemin, E.R.J., and Rosenthal, M. (2023). Structural and functional characterization of the Sin Nombre virus L protein. PLoS Pathog *19*, e1011533. 10.1371/journal.ppat.1011533.
27. Gerlach, P., Malet, H., Cusack, S., and Reguera, J. (2015). Structural Insights into Bunyavirus Replication and Its Regulation by the vRNA Promoter. Cell *161*, 1267–1279. 10.1016/j.cell.2015.05.006.
28. Arragain, B., Effantin, G., Gerlach, P., Reguera, J., Schoehn, G., Cusack, S., and Malet, H. (2020). Pre-initiation and elongation structures of full-length La Crosse virus polymerase reveal functionally important conformational changes. Nat Commun *11*, 3590. 10.1038/s41467-020-17349-4.
29. Arragain, B., Durieux Trouilleton, Q., Baudin, F., Provaznik, J., Azevedo, N., Cusack, S., Schoehn, G., and Malet, H. (2022). Structural snapshots of La Crosse virus polymerase reveal the mechanisms underlying Peribunyaviridae replication and transcription. Nat Commun *13*, 902. 10.1038/s41467-022-28428-z.
30. Wang, P., Liu, L., Liu, A., Yan, L., He, Y., Shen, S., Hu, M., Guo, Y., Liu, H., Liu, C., et al. (2020). Structure of severe fever with thrombocytopenia syndrome virus L protein elucidates the mechanisms of viral transcription initiation. Nat Microbiol *5*, 864–871. 10.1038/s41564-020-0712-2.
31. Vogel, D., Thorkelsson, S.R., Quemin, E.R.J., Meier, K., Kouba, T., Gogrefe, N., Busch, C., Reindl, S., Gunther, S., Cusack, S., et al. (2020). Structural and functional characterization of the severe fever with thrombocytopenia syndrome virus L protein. Nucleic Acids Res *48*, 5749–5765. 10.1093/nar/gkaa253.
32. Williams, H.M., Thorkelsson, S.R., Vogel, D., Milewski, M., Busch, C., Cusack, S., Grunewald, K., Quemin, E.R.J., and Rosenthal, M. (2023). Structural insights into viral genome replication by the severe fever with thrombocytopenia syndrome virus L protein. Nucleic Acids Res *51*, 1424–1442. 10.1093/nar/gkac1249.

33. Wang, X., Hu, C., Ye, W., Wang, J., Dong, X., Xu, J., Li, X., Zhang, M., Lu, H., Zhang, F., et al. (2022). Structure of Rift Valley Fever Virus RNA-Dependent RNA Polymerase. J Virol *96*, e0171321. 10.1128/JVI.01713-21.
34. Li, J., Cao, L., Zhao, Y., Shen, J., Wang, L., Feng, M., Zhu, M., Ye, Y., Kormelink, R., Tao, X., and Wang, X. (2025). Structural basis for the activation of plant bunyavirus replication machinery and its dual-targeted inhibition by ribavirin. Nat Plants *11*, 518–530. 10.1038/s41477-025-01940-y.
35. Wang, D., Yang, G., and Liu, B. (2026). Structure of Crimean-Congo haemorrhagic fever virus RNA polymerase. Nat Microbiol *11*, 1711–1721. 10.1038/s41564-026-02319-1.
36. Deng, A., Cunnison, R., Carrique, L., Gunl, F., Pardon, E., Steyaert, J., Duc, D.N., Grimes, J.M., Robb, N., and Keown, J.R. (2026). Structural and functional characterisation of the Crimean-Congo haemorrhagic fever virus RNA dependent RNA polymerase. Nat Commun. 10.1038/s41467-026-74113-w.
37. Jacques, J.-P., and Kolakofsky, D. (1991). Pseudo-templated transcription in prokaryotic and eukaryotic organisms. Genes & development *5*, 707–713.
38. CT, R.-K., and Cheng Kao, C. (2006). Biochemical Activities of the HCV NS5B RNA-Dependent RNA Polymerase. Tan SL (Hg.): Hepatitis C Viruses: Genomes and Molecular Biology. Kapitel *10*.
39. Capodagli, G.C., McKercher, M.A., Baker, E.A., Masters, E.M., Brunzelle, J.S., and Pegan, S.D. (2011). Structural analysis of a viral ovarian tumor domain protease from the Crimean-Congo hemorrhagic fever virus in complex with covalently bonded ubiquitin. J Virol *85*, 3621–3630. 10.1128/JVI.02496-10.
40. James, T.W., Frias-Staheli, N., Bacik, J.P., Levingston Macleod, J.M., Khajehpour, M., Garcia-Sastre, A., and Mark, B.L. (2011). Structural basis for the removal of ubiquitin and interferon-stimulated gene 15 by a viral ovarian tumor domain-containing protease. Proc Natl Acad Sci U S A *108*, 2222–2227. 10.1073/pnas.1013388108.
41. Pflug, A., Guilligay, D., Reich, S., and Cusack, S. (2014). Structure of influenza A polymerase bound to the viral RNA promoter. Nature *516*, 355–360. 10.1038/nature14008.
42. Reich, S., Guilligay, D., Pflug, A., Malet, H., Berger, I., Crepin, T., Hart, D., Lunardi, T., Nanao, M., Ruigrok, R.W., and Cusack, S. (2014). Structural insight into cap-snatching and RNA synthesis by influenza polymerase. Nature *516*, 361–366. 10.1038/nature14009.
43. Te Velthuis, A.J., and Fodor, E. (2016). Influenza virus RNA polymerase: insights into the mechanisms of viral RNA synthesis. Nat Rev Microbiol *14*, 479–493. 10.1038/nrmicro.2016.87.
44. Te Velthuis, A.J.W., Grimes, J.M., and Fodor, E. (2021). Structural insights into RNA polymerases of negative-sense RNA viruses. Nat Rev Microbiol *19*, 303–318. 10.1038/s41579-020-00501-8.
45. Gucwa, M., Bijak, V., Zheng, H., Murzyn, K., and Minor, W. (2024). CheckMyMetal (CMM): validating metal-binding sites in X-ray and cryo-EM data. IUCrJ *11*, 871–877. 10.1107/S2052252524007073.
46. Yuan, B., Peng, Q., Cheng, J., Wang, M., Zhong, J., Qi, J., Gao, G.F., and Shi, Y. (2022). Structure of the Ebola virus polymerase complex. Nature *610*, 394–401. 10.1038/s41586-022-05271-2.
47. Yin, W., Luan, X., Li, Z., Zhou, Z., Wang, Q., Gao, M., Wang, X., Zhou, F., Shi, J., You, E., et al. (2021). Structural basis for inhibition of the SARS-CoV-2 RNA polymerase by suramin. Nat Struct Mol Biol *28*, 319–325. 10.1038/s41594-021-00570-0.
48. Mastrangelo, E., Pezzullo, M., Tarantino, D., Petazzi, R., Germani, F., Kramer, D., Robel, I., Rohayem, J., Bolognesi, M., and Milani, M. (2012). Structure-based inhibition of Norovirus RNA-dependent RNA polymerases. J Mol Biol *419*, 198–210. 10.1016/j.jmb.2012.03.008.
49. Jiao, L., Ouyang, S., Liang, M., Niu, F., Shaw, N., Wu, W., Ding, W., Jin, C., Peng, Y., Zhu, Y., et al. (2013). Structure of severe fever with thrombocytopenia syndrome virus nucleocapsid protein in complex with suramin reveals therapeutic potential. J Virol *87*, 6829–6839. 10.1128/JVI.00672-13.
50. Ellenbecker, M., Lanchy, J.M., and Lodmell, J.S. (2014). Inhibition of Rift Valley fever virus replication and perturbation of nucleocapsid-RNA interactions by suramin. Antimicrob Agents Chemother *58*, 7405–7415. 10.1128/AAC.03595-14.
51. Boehr, D.D., Nussinov, R., and Wright, P.E. (2009). The role of dynamic conformational ensembles in biomolecular recognition. Nat Chem Biol *5*, 789–796. 10.1038/nchembio.232.
52. Johnson, S., Henschke, N., Maayan, N., Mills, I., Buckley, B.S., Kakourou, A., and Marshall, R. (2018). Ribavirin for treating Crimean Congo haemorrhagic fever. Cochrane Database Syst Rev *6*, CD012713. 10.1002/14651858.CD012713.pub2.

53. Ascioglu, S., Leblebicioglu, H., Vahaboglu, H., and Chan, K.A. (2011). Ribavirin for patients with Crimean-Congo haemorrhagic fever: a systematic review and meta-analysis. J Antimicrob Chemother *66*, 1215–1222. 10.1093/jac/dkr136.
54. Hawman, D.W., Haddock, E., Meade-White, K., Nardone, G., Feldmann, F., Hanley, P.W., Lovaglio, J., Scott, D., Komeno, T., Nakajima, N., et al. (2020). Efficacy of favipiravir (T-705) against Crimean-Congo hemorrhagic fever virus infection in cynomolgus macaques. Antiviral Res *181*, 104858. 10.1016/j.antiviral.2020.104858.
55. Tipih, T., Meade-White, K., Rao, D., Bushmaker, T., Lewis, M., Shaia, C., Feldmann, H., and Hawman, D.W. (2023). Favipiravir and Ribavirin protect immunocompetent mice from lethal CCHFV infection. Antiviral Res *218*, 105703. 10.1016/j.antiviral.2023.105703.
56. Hawman, D.W., Haddock, E., Meade-White, K., Williamson, B., Hanley, P.W., Rosenke, K., Komeno, T., Furuta, Y., Gowen, B.B., and Feldmann, H. (2018). Favipiravir (T-705) but not ribavirin is effective against two distinct strains of Crimean-Congo hemorrhagic fever virus in mice. Antiviral Res *157*, 18–26. 10.1016/j.antiviral.2018.06.013.
57. Ji, X., Jiang, X., Huang, X., Gao, H., Gao, Z., Gao, P., De Clercq, E., Pannecouque, C., Kang, D., Zhan, P., and Liu, X. (2025). Design, synthesis, and biological evaluation of dual-site HIV-1 inhibitors simultaneously targeting the NNRTI binding pocket and an adjacent site with favorable resistance profiles. Bioorg Chem *164*, 108924. 10.1016/j.bioorg.2025.108924.
58. Pettersen, E.F., Goddard, T.D., Huang, C.C., Meng, E.C., Couch, G.S., Croll, T.I., Morris, J.H., and Ferrin, T.E. (2021). UCSF ChimeraX: Structure visualization for researchers, educators, and developers. Protein Sci *30*, 70–82. 10.1002/pro.3943.
59. Punjani, A., Rubinstein, J.L., Fleet, D.J., and Brubaker, M.A. (2017). cryoSPARC: algorithms for rapid unsupervised cryo-EM structure determination. Nat Methods *14*, 290–296. 10.1038/nmeth.4169.
60. Casanal, A., Lohkamp, B., and Emsley, P. (2020). Current developments in Coot for macromolecular model building of Electron Cryo-microscopy and Crystallographic Data. Protein Sci *29*, 1069–1078. 10.1002/pro.3791.
61. Afonine, P.V., Poon, B.K., Read, R.J., Sobolev, O.V., Terwilliger, T.C., Urzhumtsev, A., and Adams, P.D. (2018). Real-space refinement in PHENIX for cryo-EM and crystallography. Acta Crystallogr D Struct Biol *74*, 531–544. 10.1107/S2059798318006551.
62. Abramson, J., Adler, J., Dunger, J., Evans, R., Green, T., Pritzel, A., Ronneberger, O., Willmore, L., Ballard, A.J., Bambrick, J., et al. (2024). Accurate structure prediction of biomolecular interactions with AlphaFold 3. Nature *630*, 493–500. 10.1038/s41586-024-07487-w.

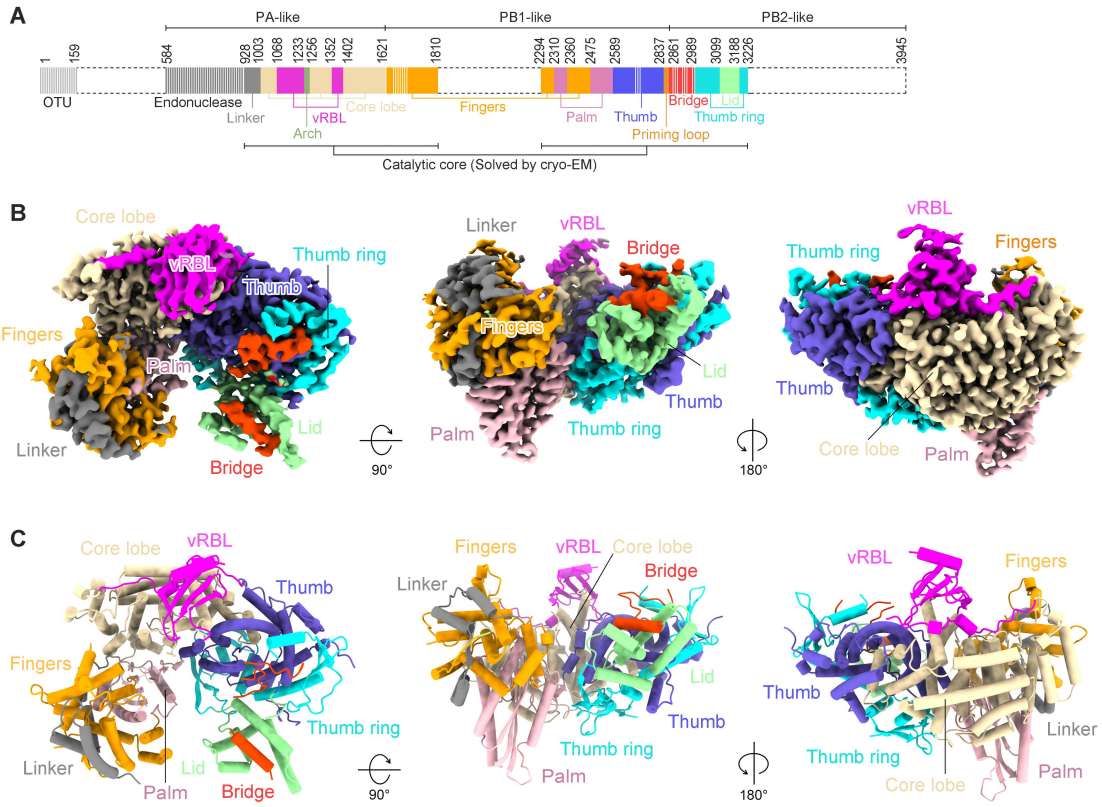
A
PA-like
PB1-like
PB2-like
1
159
584
928
1003
1068
1233
1256
1352
1402
1621
1810
2294
2310
2360
2475
2589
2837
2861
2989
3099
3188
3226
3945
OTU
Endonuclease
Linker
vRBL
Arch
Core lobe
Fingers
Palm
Thumb
Bridge
Lid
Thumb ring
Priming loop
Catalytic core (Solved by cryo-EM)
B
Core lobe
vRBL
Thumb ring
Thumb
Fingers
Palm
Linker
Lid
Bridge
90°
Linker
vRBL
Bridge
Fingers
Lid
Thumb
Palm
Thumb ring
180°
vRBL
Thumb ring
Fingers
Thumb
Core lobe
Palm
C
Core lobe
vRBL
Thumb
Fingers
Thumb ring
Linker
Lid
Palm
Bridge
90°
Fingers
vRBL
Core lobe
Linker
Bridge
Lid
Thumb
Thumb ring
Palm
180°
vRBL
Fingers
Thumb
Linker
Thumb ring
Core lobe
Palm

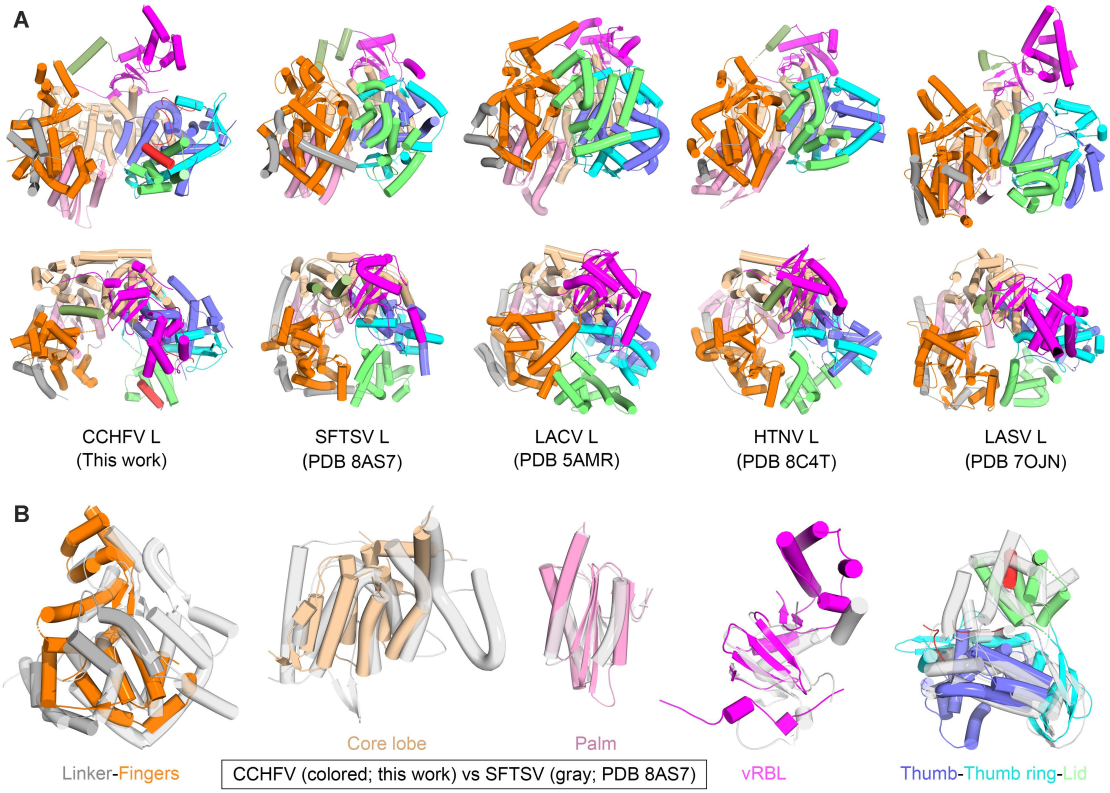
A
CCHFV L
(This work)
SFTSV L
(PDB 8AS7)
LACV L
(PDB 5AMR)
HTNV L
(PDB 8C4T)
LASV L
(PDB 7OJN)
B
Linker-Fingers
Core lobe
Palm
vRBL
Thumb-Thumb ring-Lid
CCHFV (colored; this work) vs SFTSV (gray; PDB 8AS7)
C
motif H2399-2403
2517DD2518
motif G1523-1533
motif B2474-2489
motif E2573-2583
PR loop2307-2316
motif D2560-2572
motif C2506-2529
motif A2346-2367
D
C1065
C1028
Zn2+
C1062
C1031
H1365
C1294
Zn2+
E2788
H1090
G2357
Mn2+
E2575
D2518
E1430
R1427
Mg2+
E3081
N3083

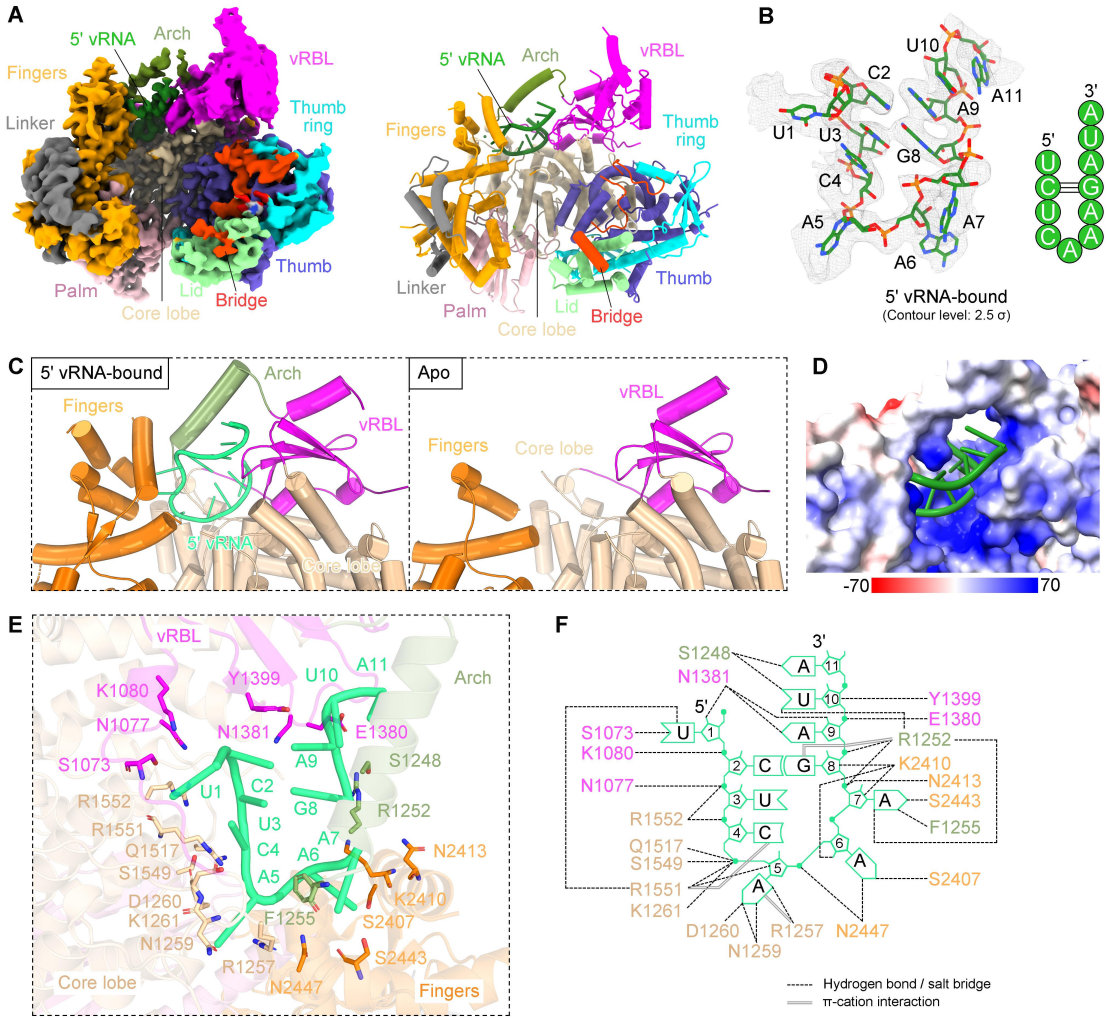
A
5' vRNA
Arch
Fingers
vRBL
Linker
Thumb ring
Thumb
Palm
Lid
Bridge
Core lobe
B
U10
C2
A11
A9
U1
U3
G8
C4
A5
A7
A6
5'
3'
5' vRNA-bound
(Contour level: 2.5 σ)
C
5' vRNA-bound
Apo
Fingers
Arch
vRBL
Core lobe
D
-70
70
E
vRBL
K1080
Y1399
U10
A11
Arch
N1077
N1381
E1380
S1073
A9
S1248
R1552
U1
C2
G8
R1252
R1551
U3
A7
Q1517
C4
A6
N2413
S1549
A5
D1260
K1261
F1255
K2410
S2407
N1259
R1257
S2443
Core lobe
N2447
Fingers
F
S1248
N1381
3'
5'
S1073
K1080
N1077
R1552
R1551
Q1517
S1549
K1261
D1260
N1259
R1257
N2447
Y1399
E1380
R1252
K2410
N2413
S2443
F1255
S2407
Hydrogen bond / salt bridge
π-cation interaction

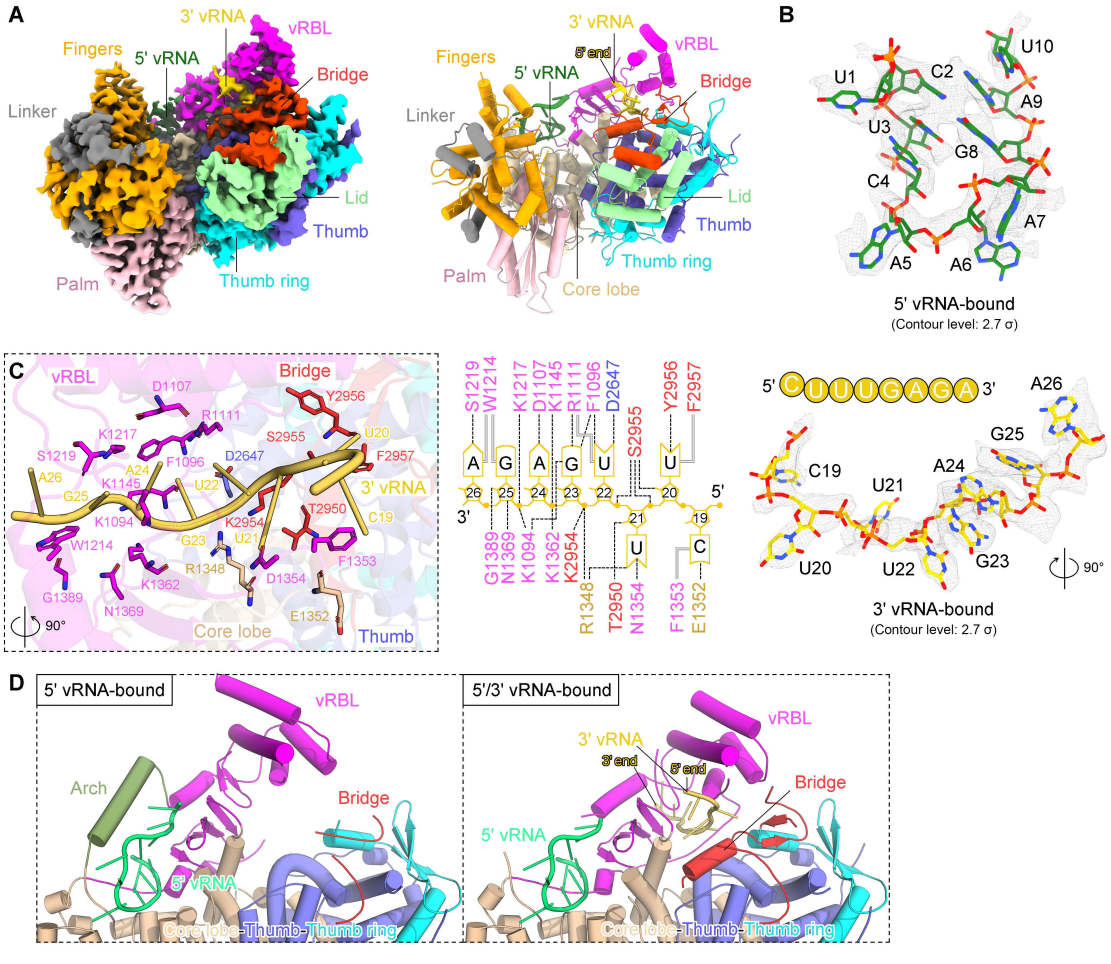
A
3' vRNA
vRBL
Fingers
5' vRNA
Bridge
Linker
Lid
Thumb
Palm
Thumb ring
5' end
Core lobe
B
U10
U1
C2
A9
U3
G8
C4
A7
A5
A6
5' vRNA-bound
(Contour level: 2.7 σ)
C
D1107
R1111
K1217
S1219
F1096
D2647
A26
A24
K1145
U22
G25
K1094
K2954
W1214
G23
U21
R1348
K1362
G1389
N1369
D1354
T2950
F1353
E1352
90°
Core lobe
Thumb
S1219
W1214
K1217
D1107
K1145
R1111
F1096
D2647
S2955
Y2956
F2957
A
G
A
G
U
U
26
25
24
23
22
21
20
19
5'
3'
U
C
G1389
N1369
K1094
K1362
K2954
R1348
T2950
N1354
F1353
E1352
5' C U U U C A G A 3'
A26
G25
C19
U21
A24
U20
U22
G23
90°
3' vRNA-bound
(Contour level: 2.7 σ)
D
5' vRNA-bound
vRBL
Arch
Bridge
3' vRNA
Core lobe-Thumb-Thumb ring
5'/3' vRNA-bound
3' vRNA
3' end
5' end
vRBL
Bridge
5' vRNA
Core lobe-Thumb-Thumb ring

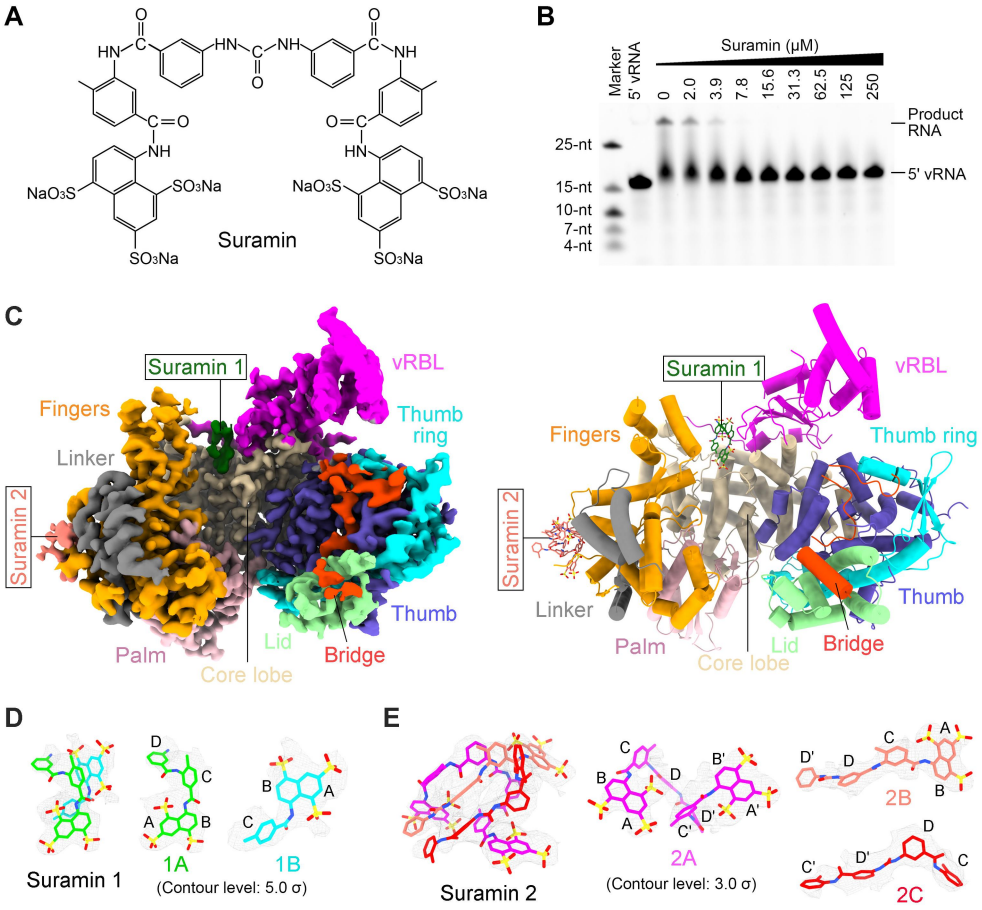
A
Suramin
B
Marker
5' vRNA
Suramin (μM)
0
2.0
3.9
7.8
15.6
31.3
62.5
125
250
25-nt
15-nt
10-nt
7-nt
4-nt
Product RNA
5' vRNA
C
Suramin 1
vRBL
Fingers
Thumb ring
Linker
Suramin 2
Thumb
Palm
Lid
Bridge
Core lobe
D
Suramin 1
1A
1B
(Contour level: 5.0 σ)
E
Suramin 2
2A
2B
2C
(Contour level: 3.0 σ)

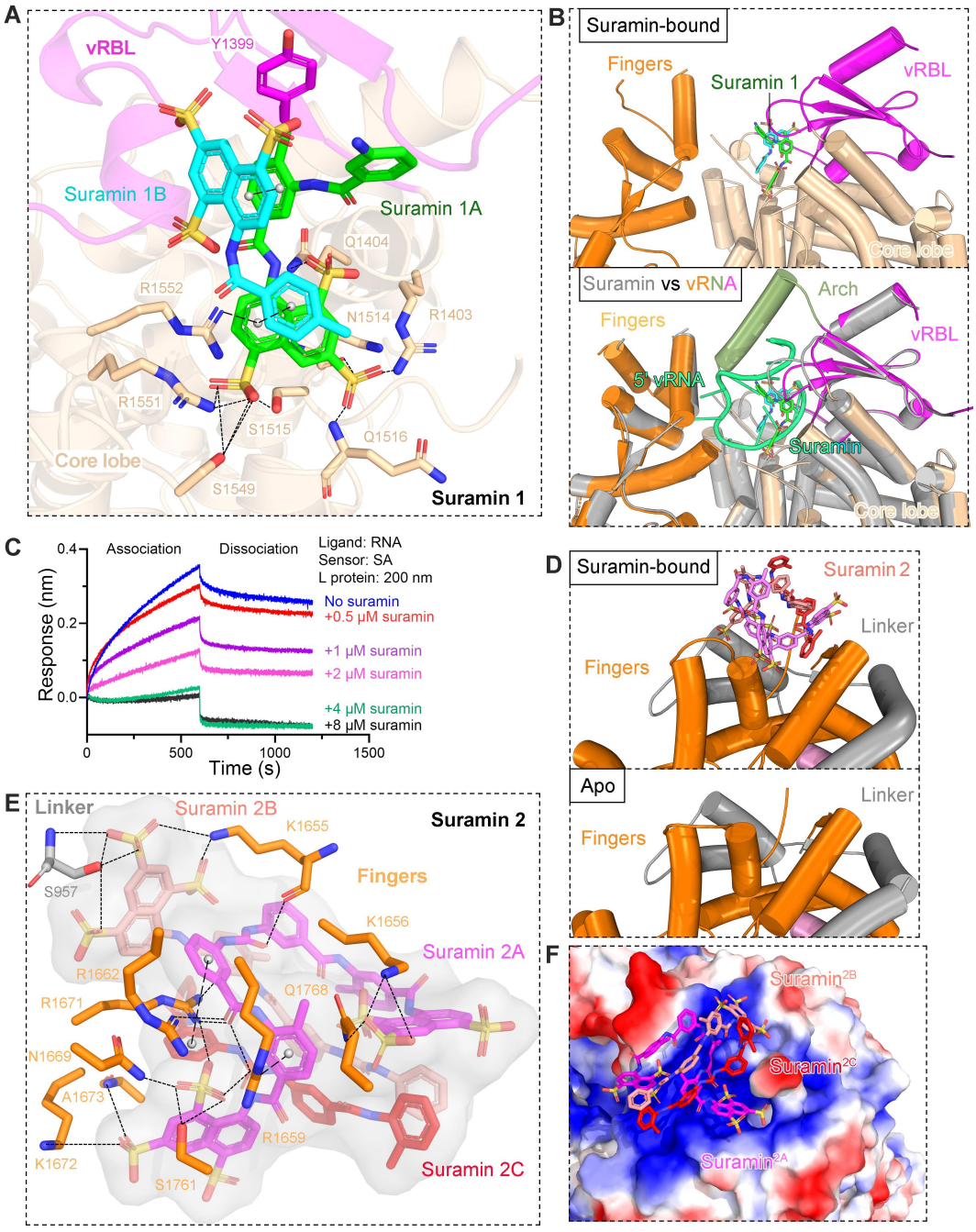
A
vRBL
Y1399
Suramin 1B
Suramin 1A
Q1404
R1552
N1514
R1403
R1551
S1515
Q1516
Core lobe
S1549
Suramin 1
B
Suramin-bound
Fingers
Suramin 1
vRBL
Core lobe
Suramin vs vRNA
Arch
Fingers
vRBL
5' vRNA
Suramin
Core lobe
C
Association
Dissociation
Ligand: RNA
Sensor: SA
L protein: 200 nm
No suramin
+0.5 μM suramin
+1 μM suramin
+2 μM suramin
+4 μM suramin
+8 μM suramin
Response (nm)
Time (s)
D
Suramin-bound
Suramin 2
Linker
Fingers
Apo
Linker
Fingers
E
Linker
Suramin 2B
Suramin 2
K1655
Fingers
S957
K1656
Suramin 2A
R1662
Q1768
R1671
N1669
A1673
R1659
K1672
S1761
Suramin 2C
F
Suramin2B
Suramin2C
Suramin2A

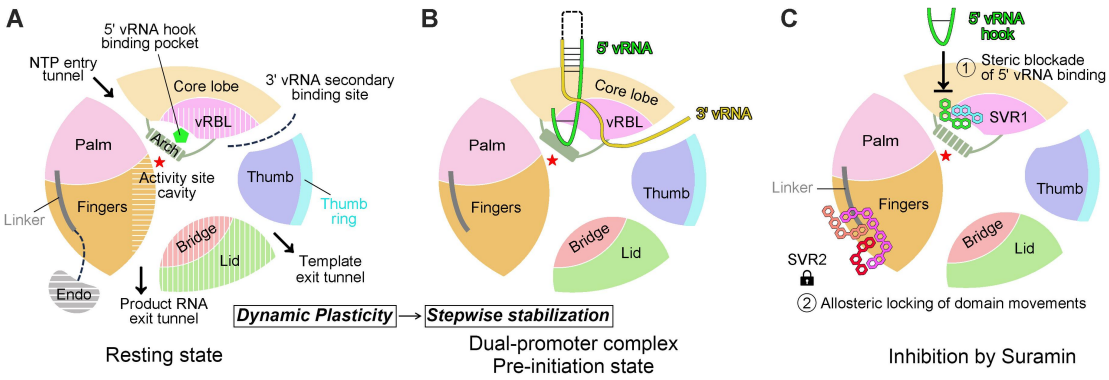
A
5' vRNA hook binding pocket
NTP entry tunnel
Core lobe
3' vRNA secondary binding site
vRBL
Palm
Arch
Activity site cavity
Thumb
Thumb ring
Linker
Fingers
Bridge
Lid
Template exit tunnel
Endo
Product RNA exit tunnel
Resting state
B
5' vRNA
Core lobe
3' vRNA
vRBL
Palm
Fingers
Thumb
Bridge
Lid
Dual-promoter complex
Pre-initiation state
C
5' vRNA hook
① Steric blockade of 5' vRNA binding
SVR1
Palm
Linker
Fingers
Thumb
Bridge
Lid
SVR2
② Allosteric locking of domain movements
Inhibition by Suramin
Dynamic Plasticity
Stepwise stabilization